universität wien

MASTERARBEIT / MASTER'S THESIS

Titel der Masterarbeit / Title of the Master's Thesis

„Measurement of electron irradiation damage in two-dimensional hexagonal boron nitride“

verfasst von / submitted by

Thi Thuy An Bui, BSc

angestrebter akademischer Grad / in partial fulfilment of the requirements for the degree of

Master of Science (MSc)

Wien, 2020 / Vienna, 2020

Studienkennzahl lt. Studienblatt / degree programme code as it appears on the student record sheet:	A 066 876
Studienrichtung lt. Studienblatt / degree programme as it appears on the student record sheet:	Masterstudium Physik UG2002
Betreut von / Supervisor:	Assoz. Prof. Dr. Jani Kotakoski

Abstract

A highly energetic electron beam in a scanning transmission electron microscope (STEM) can transfer enough energy to cause damage to specimens. However, created defects may not always be detrimental. Thus, a fundamental understandig of beam induced defects in two-dimensional (2D) materials such as graphene, MoS_2 or hexagonal boron nitride (hBN) can be benefical due to their fascinating properties. Knock-on and radiolysis are two dominant mechanisms to create defects, when electrons interact with materials. Earlier studies established that in a metallic specimen such as graphene, only the knock-on damage caused by elastically scattered electrons, plays a role. However, in semiconducting materials such as MoS_2 or insulators like hBN, the aspect of both damage mechanisms has to be considered. Moreover, the damage mechanism under electron irradiation is not fully understood. In this thesis, aberration-corrected STEM was employed to study the damage mechanism in free-standing hBN monolayers. The samples were prepared by transferring chemical vapor deposition (CVD) grown flakes directly on top of TEM grids. Experiments were conducted using various acceleration voltages (55, 60, 70, 80 kV). Atomically resolved imaging revealed the defect configurations of single B or N atoms in monolayer hBN. Suprisingly, we also observed occasionally the ejection of N atom as first vacancy in the frame, which is not favored to happen from theory. Statistical analysis of damage rate as a function of the electron dose is done at different acceleration voltages using various magnification. We compared the experimental cross section values with theoretical predictions. Our results show that both knock-on and radiolysis are responsible for defect creation in single layer hBN.

Zusammenfassung

In einem Rastertransmissionselektronenmikroskop (STEM) können hochenergetische Elektronenstrahlen, bei ausreichendem Energieübertrag auf eine Probe, zu einer Beschädigung dieser führen. Diese Veränderung ist nicht immer zwangsweise als schädlich zu betrachten. Ein fundamentales Verständnis von Elektronenstrahlen verursachten Defekten in zweidimensionalen (2D) Materialien, wie Graphen, MoS_2 oder hexagonales Bornitrid (hBN), ist daher von großer Bedeutung. Bei der Interaktion mit dem Material, sind 'Knock-on' und die Radiolyse zwei dominante Mechanismen um Defekte zu erzeugen. Frühere Studien zeigten, dass in metallischen Proben wie Graphen, nur die 'Knock-on' Schädigung, welches durch den elastischen Stoß mit einfallenden Elektronen verursacht wird, eine Rolle spielt. Allerdings müssen in Halbleitern wie MoS_2 oder Isolatoren wie hBN beide Mechanismen berücksichtigt werden. Das Verständnis des Mechanismus, der durch Elektronenstrahlen verursachte Defekte erzeugt, ist noch unklar. In dieser Arbeit wurde unter Verwendung eines Aberrationen korrigierten STEM, der Schädigungsmechanismus in einem frei-stehenden, einlagigen hBN, untersucht. Die Probe wurde durch einen direkten Transfer von einer durch chemische Gasphasenabscheidung (CVD) gewachsenen Flocke auf die Oberfläche eines 'TEM Grids', hergestellt. Die Experimente wurden bei verschiedenen Beschleunigungsspannungen (55, 60, 70, 80 kV) durchgeführt. Atomar aufgelöste Bilder offenbaren Konfigurationen von Defekten einzelner Bohr- oder Stickstoffatomen in einer Schicht hBN. Überraschenderweise konnten wir per Zufall das Ausschlagen von Stickstoff Atomen als einen ersten Defekt beobachten. Dies ist aufgrund der Theorie allerdings kein begünstigter Vorgang. Die Rate der Beschädigungen wurde statistisch mit einer Funktion der Elektronendosis bei verschiedenen Beschleunigungsspannungen und verschiedenen Vergrößerungen, analysiert. Wir verglichen auch die experimentellen Werte der Wirkungsquerschnitte mit deren theoretischen Vorhersagen. Als Ergebnis konnte gezeigt werden, dass für die Defektbildung in einem einlagigen hBN beide Mechanismen, 'Knock-on' und Radiolyse verantwortlich ist.

Contents

1 Introduction **5**

2 Materials **7**

2.1 Hexagonal Boron-Nitride (hBN) 7

2.2 Sample preparation 10

3 Methods **14**

3.1 Scanning Transmission Electron Microscopy (STEM) 14

3.1.1 Aberrations 18

3.1.2 Imaging 20

3.2 Electron-irradiation damage 22

3.2.1 (Displacement) Cross section 23

3.2.2 Elastic scattering 25

3.2.3 Inelastic scatterring 27

4 Results and Discussion **29**

4.1 Image analysis 30

4.1.1 Single vacancy 32

4.1.2 Other defects 34

4.1.3 Dose until first defect 35

4.2 Statistical analysis 35

4.3 Experimental determination of σ 36

4.4 Exponential fits of a Poisson process 39

4.4.1 σ for combined B & N electron doses with different FOVs 39

4.4.2 σ separately for B & N 43

4.5 Radiolysis 48

5 Conclusions **50**

Chapter 1

Introduction

Isolation of a single sheet of graphene in 2004 [1] indicated that two-dimensional (2D) materials can exist at finite temperatures [2]. Indeed, inorganic 2D systems such as individual hexagonal boron nitride (hBN) [3, 4] and transition metal dichalcogenide (TMD) layers [3, 4, 5, 6, 7, 8] were later manufactured by mechanical [3, 5] and chemical [6, 4] exfoliation of their layered bulk counterparts, as well as by chemical vapor deposition [7, 8]. Characterization of 2D materials including hBN and TMDs have extensively been carried out using high-resolution transmission electron microscopy (HR-TEM). However, the materials can damage due to the interaction with the electron beam.

For example, energetic electrons in a TEM can give rise to production of defects due to ballistic displacements of atoms from the sample, electronic excitations, ionization and beam-induced chemical etching, as studies on hBN membranes also indicate [9, 10]. The displacement threshold energy (T_d) signifies the minimum amount of kinetic energy required to eject an atom from its lattice position in a crystal [11, 12] and is sufficient to fully describe ballistic displacements (so called knock-on damage). These two above mentioned damage mechanism will be explained in more details in Chapter 2.

Ionization damage (radiolysis) and knock-on displacement can be compared in terms of scattering cross section [13, 14, 15] and stopping power, for thin specimens exposed to electrons in a TEM. The mechanism of radiation damage in beam-sensitive TEM specimens is of practical interest because it determines what options are available for minimizing the damage. If radiolysis is the main damage process, cooling the specimen by liquid N_2 or He can reduce the damage by typically a factor of 3-10 [16]. If knock-on displacement is predominant, reducing the TEM acceleration

voltage below some threshold value will largely lower the damage. If the damaging effects arise from beam heating or from electrostatic charging of an insulating specimen, reducing the incident beam current can be helpful [16].

In inorganic solids, both knock-on and radiolysis effects can take place, sometimes simultaneously. Radiolysis is predominant in insulators. In conducting samples, radiolysis is largely quenched, leaving knock-on displacement as the only damage mechanism. In organic materials, cross sections for knock-on displacement are generally smaller, and the characteristic dose correspondingly larger in contrast to the radiolysis damage [16].

In early experiments with graphene [17], time series of displacement of carbon atoms were recorded at room temperature using HR-TEM. The atomic displacement knock-on cross section by counting the electron-beam-induced displacements of single carbon atoms.

Additional work has been done using STEM [18], where each atom, or its loss, was visible in every frame [19]. From each experimental dataset, a clear displacement was observed and the accumulated electron dose was calculated until the frame where the first defect appeared. The distribution of doses follows a Poisson process and the corresponding expectation value was found by log-likelihood minimization. With this the probability to create a vacancy can be calculated. Although these results were achieved with graphene, this technique should work for any low-dimensional material, including hBN and TMDs [19]. Experimental studies were done with MoS_2 [15, 9].

This thesis presents an accurate measurement and a quantitative analysis of electron-beam-induced displacements in single-layer hBN. Preparation of the hBN samples is also included in this work. This was achieved by transferring CVD-grown monolayer hBN onto a TEM grid. To measure the probability to create defects in hBN, image series were recorded with Nion UltraSTEM100 at different acceleration voltages between 55-80 kV. Atomically resolved imaging revealed directly the defect positions in hBN lattice. Interestingly, a frequent ejection of N atom as first vacancy in the frame, which is not favored to happen from the theory, will also be shown. The accumulated electron doses and the displacement cross sections are calculated for hBN. Comparing these results to theoretical damage models leads to a better understanding of ionization damage under electron irradiation in 2D materials.

Chapter 2

Materials

In a direct contrast to their bulk counterparts, the structure of 2D materials are different and thus attract more attention to the fundamental research. For a long time they were believed to be structurally unstable because of long-wavelength fluctuations according to the Mermin-Wagner theorem [20]. However, a whole new research field opened after Konstantin Novoselov and Andre Geim exfoliated single-layer graphene for the first time [1], which followed with a Nobel prize in physics in 2010. 2D materials including graphene, hBN and TMDs have unique physical properties which leads to many promising applications.

2.1 Hexagonal Boron-Nitride (hBN)

hBN is considered to have a mixed covalent-ionic bonding. A covalent bond is a bond where electrons are shared roughly equally between two atoms, whereas ionic bonding occurs between oppositely charged ions [21]. Single layer hexagonal boron nitride (hBN) is considered the thinnest possible 2D crystal with slightly ionic bonds. This characteristic makes atomically thin hBN an ideal model system to study atomic configurations, including defects and edges of 2D ionic crystals [22]. It is also known as a very good electrical insulator with good thermal conductivity and stability [23].

On the right of the second row of the periodic table are B, N, C, O, F, Ne which have electron configuration $1s^2\ 2s^2\ 2p^x$ with $x = 1...6$ because the $2p$ shell can hold at most 6 electrons. Hence, the electron configuration for boron is $1s^2\ 2s^2\ 2p^1$, and for nitrogen is $1s^2\ 2s^2\ 2p^3$.

Atomic structure of hBN consists of two-dimensional layers of hexagons with a weak interaction

between the different layers (van der Waals interaction). The alternating boron and nitrogen atoms are sp^2-bonded to each other. sp^2 hybridisation is a mixture of one s and two p orbitals of the same shell forming three equivalent orbitals, which leads to a triangular shape. Between the layers boron and nitrogen atoms are stacked on top of each other [24, 10].

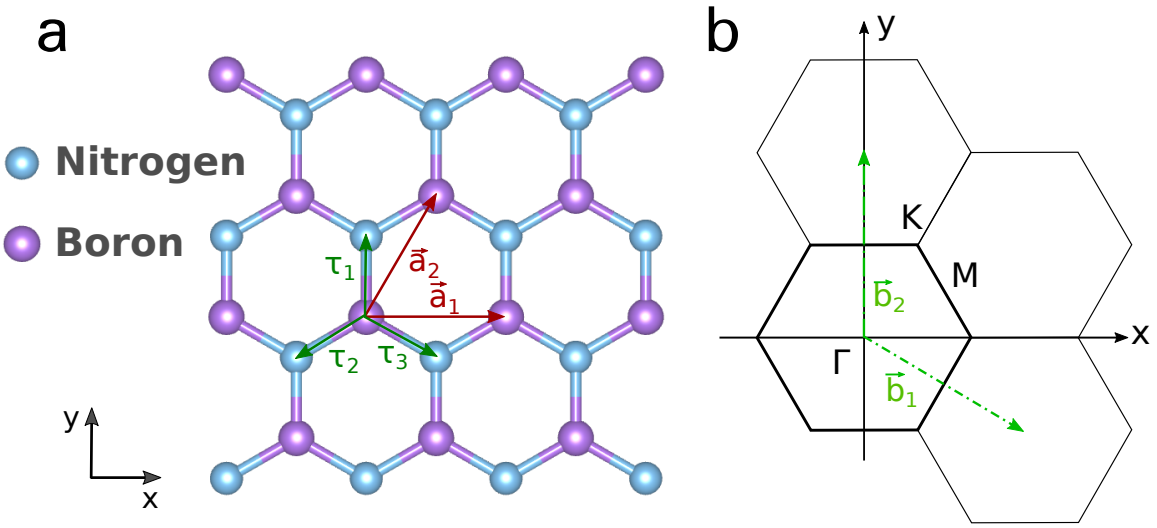

Figure 2.1: **Atomic structure of hBN.** (a) Schematic illustration of one layer of hBN. (b) Two-dimensional Brillouin zone for hBN. Γ, M and K are high-symmetry points.

Figure 2.1 shows the crystal structure of hBN. Since this thesis focused on single layer hBN, the structure of bulk hBN will not be discussed further here. A detailed description of a three-dimensional crystal structure of BN can be found in Reference [24]. The distance between the neighbouring boron and nitrogen atoms is $\tau_1 = \tau_2 = \tau_3 = 1.45$ Å. $\vec{a}_1$, $\vec{a}_2$ are the primitive vectors of a 2D hexagonal lattice:

$$\vec{a}_1 = a \begin{pmatrix} 1 \\ 0 \\ 0 \end{pmatrix}, \qquad \vec{a}_2 = \frac{a}{2} \begin{pmatrix} 1 \\ \sqrt{3} \\ 0 \end{pmatrix}. \tag{2.1}$$

The value of the lattice constant is $a = 2.504$ Å.

The reciprocal lattice provides a simple geometrical basis for understanding wave nature phenomena, like the behaviour of electrons and lattice vibrations in crystals. It is also useful for measuring the geometry of x-ray and electron diffraction patterns.

Using a common origin for both reciprocal and direct lattices, we can build up the reciprocal

lattice with the reciprocal vectors $\vec{b}_1$, $\vec{b}_2$.

$$\vec{b}_1 = \frac{2\pi}{a}\begin{pmatrix} 1 \\ -\frac{1}{\sqrt{3}} \\ 0 \end{pmatrix}, \qquad \vec{b}_2 = \frac{2\pi}{a}\begin{pmatrix} 0 \\ \frac{2}{\sqrt{3}} \\ 0 \end{pmatrix}. \tag{2.2}$$

The corresponding Brillouin zone is shown in Figure 2.1 b, including the high-symmetry points Γ, K and M.

The energy bands and optical properties of h-BN in 2D and 3D have been calculated theoretically by using the tight-binding model in a semi-empirical approach [24]. At the point K of the Brillouin zone the energy gap is approximately equal to the difference in the energies of the $2p$ states of the atoms constituting the lattice. Experiments showed that h-BN has a direct-gap with a bandgap energy of 5.971 eV [25]. With the Young's modulus which is a mechanical property, the stiffness of a solid material can be described. An experimental value of the elastic modulus (Young's modulus) for monolayer hBN is 0.865 ± 0.073 TPa. It also has a fracture strength of 70 ± 5.5 GPa [26].

2.2 Sample preparation

Transmission electron microscopy samples have to be thin enough so that they can be traversed by the imaging electrons. Generally, this requirement is a function of the electron energy and the average atomic number (Z) of your specimen.

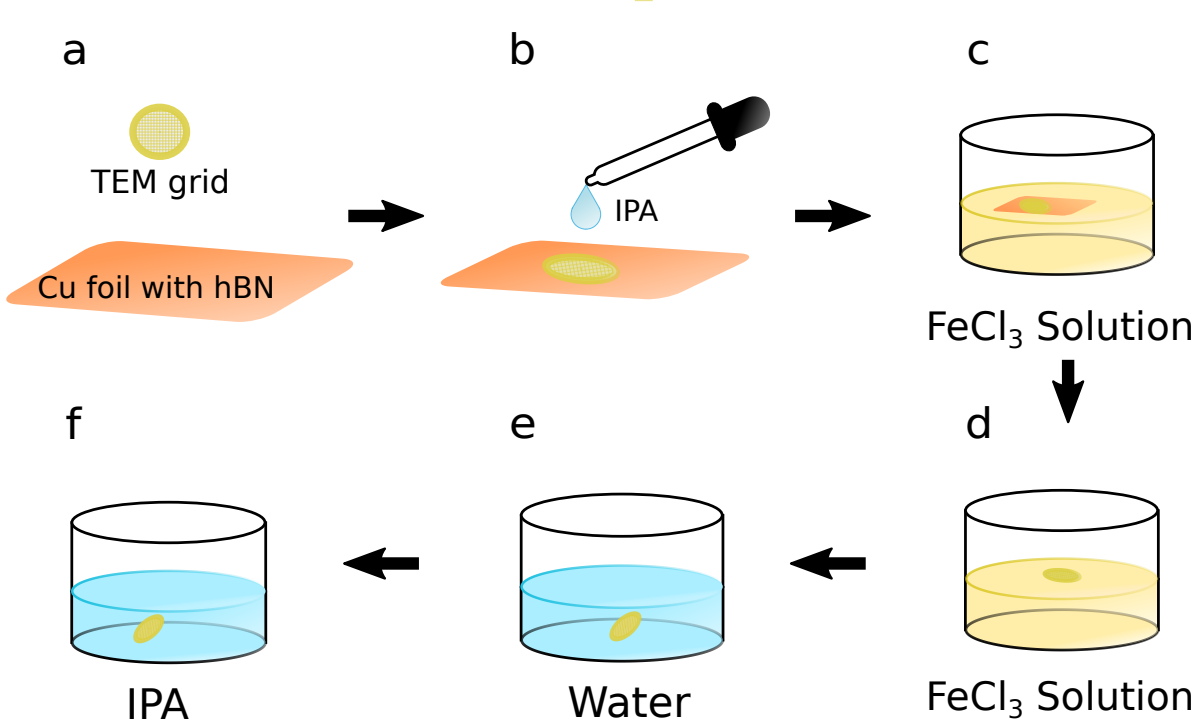

Figure 2.2: **Sample preparation.** a) Gold TEM grid and CVD grown h-BN on Cu foil. (b) Attaching TEM grid onto the Cu foil with isopropanol (IPA). (c) TEM grid on top of the Cu foil on the surface of a $FeCl_3$ solution. (d) Solution left with sample (TEM grid) after some days. (e)-(f) Cleaning of the sample with water and IPA.

Figure 2.2 shows a schematic of the sample preparation process. Before we can make any experiments we need, a suitable sample with the material of interest. In our case, it is monolayer hBN. We bought commercial monolayer hBN from graphene-supermarket.com [27]. They used the CVD method [7] to sythesize it on a copper foil. To transfer the sample, a conventional TEM gold grid covered with an amourphous carbon film with holes (Quantifoil R 1.2/1.3, grid: Au 200) is placed on top of the copper foil coated with a monolayer hBN (Fig. 2.2 a).

During the transfer process, to avoid mechanical damage to the sample or fragil grids, one needs to be very careful. A TEM grid on top of a CVD grown monolayer hBN can be seen in Figure 2.3

a. To attach the TEM grids onto hBN, one drop of isopropanol (IPA) is put on top of the already placed grid (Fig. 2.2 b). During evaporation of the IPA drop, we used a light microscope to check the adhesion process (Fig. 2.3 b). For a successful transfer, uniform adhesion between the substrate and the TEM grid is necessary. If the Cu foil or TEM grid is not flat due to mishandeling or mechanical damage, then there will not be full adhesion. This can be seen in Figure 2.3 b. Darker squared If it is not properly adhered, then few more drops of IPA can be used to improve adhesion. After the evaporation of IPA, we checked that the TEM grid remains properly attached to the substrate (Fig. 2.3). Figure 2.3 c shows a zoomed in image of an attached area with four full and two half squares. The middle square in the first row is almost fully attached to the Cu foil with the hBN monolayer. An example with a not fully attached case is shown in the second row also the middle quare. On the top and bottom corner on the left side of the quare there are brighter contrast regions than in the middle.

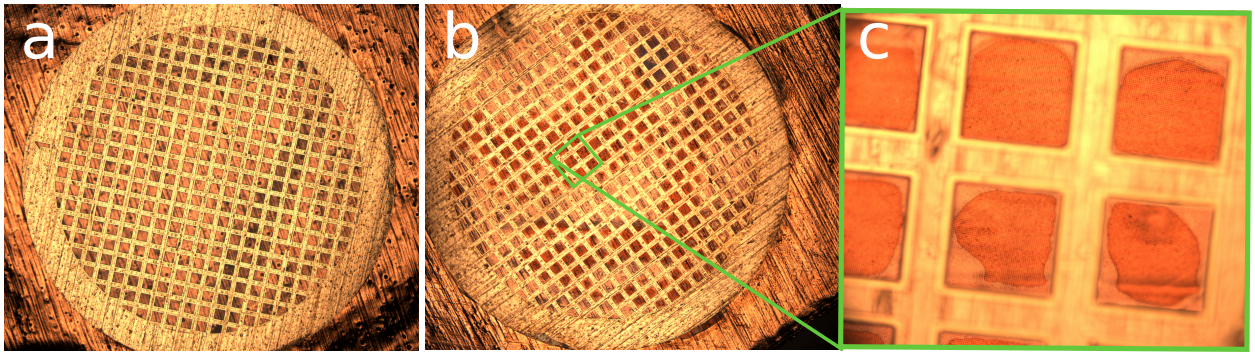

Figure 2.3: **Adhesion of hBN on TEM grid.** Light Microscope images. (a) TEM grid on top of CVD growth monolayer hBN. (b) TEM grid on top of CVD growth monolayer hBN after adhesion process with evaporated IPA drops. Dark squares are atteched regions. (c) Zoomed in image of several dark squares, showing attached regions.

To remove the copper foil, to get only the TEM grid with the adhesed hBN, it needs to be etched. To etch a Cu foil, an acid solution, e.g. iron(III)-chloride ($FeCl_3$) can be used. The $FeCl_3$ solvent concentration shouldn't be too high in order not to damage the sample. We found high success rate with the sample transfer at 10 % concentration. In Fig. 2.2 c, the copper foil with the attached grid is carefully put on to the surface of the glass beaker with the $FeCl_3$ solution. With this solvent concentration, it takes 3-5 days to fully etch the Cu foil. Afterwards, the TEM grid starts floating on the surface as shown in Fig. 2.2 d. To get rid of chemical residues, we need to clean the sample. Contamination is a well known problem for 2D materials as it prevents

atomic resolution in transmission electron microscopy. To minimize this issue, samples should be cleaned properly. First, we cleaned the sample with deionised (DI) water for 60 s in a beaker and then repeated the same process in another beaker with fresh DI water. Finally, to make sure that the sample is completely dry, we put the TEM grid into a beaker filled with IPA, as shown in Fig 2.2 e & f.

hBN samples were prepared two times with the above mentioned process. First time, copper foil with the TEM grid on top were left in the solution for 5 days, and the second time for 3 days to check if there is difference in the sample quality. Figure 2.4 a shows an image of the sample, recorded with a charge-coupled device (CCD) camera. Many small black (dark contrast) regions can be seen, which are most likely Fe clusters coming from the residues of the $FeCl_3$ solvent. In contrast, Fig. 2.4 b looks cleaner and there is no sign of Fe at this magnification.

Figure 2.4 c & d show scanning transmission electron microscopy (STEM) images recorded with a medium angle annular dark field (MAADF) detector. Images in this mode have opposite contrast to the CCD mode, i.e. the dark clusters are bright now. In MAADF images, Fe clusters appear bright (see Fig 2.4 c). The dark areas are the clean regions and the brighter but not white are contaminated areas. The second samples, that looks cleaner in the overview images actually has less clean areas in the MAADF images. It also has many small bright contrast conatminations and many atomically small holes (see Fig. 2.4 d), so that its more difficult to find a good clean region. Therefore, sample one was preferential used for our experiments.

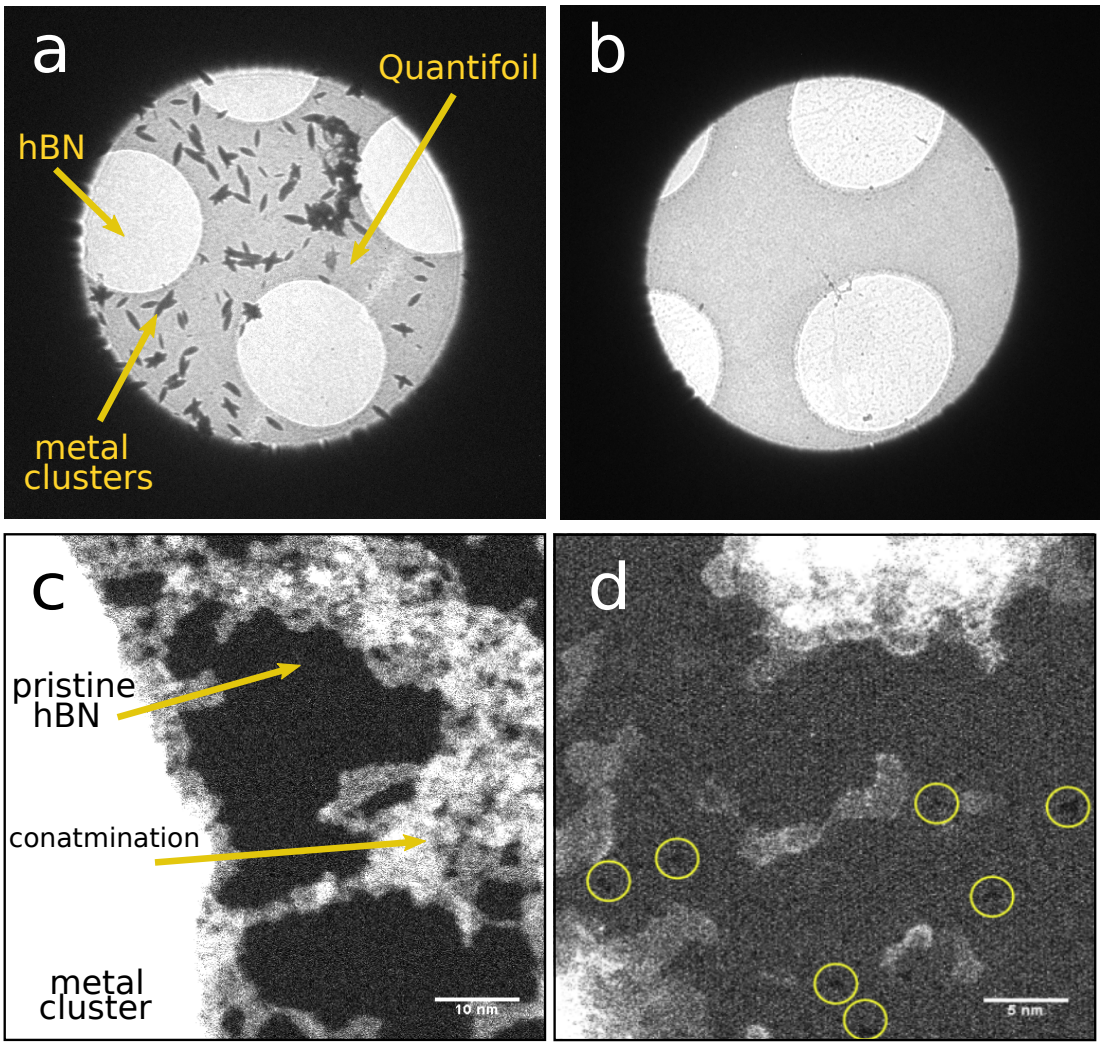

Figure 2.4: **STEM images of transferred samples using two different conditions.** (a)-(b) CCD images. (c)-(d) MAADF images. Samples of monolayer hBN were in $FeCl_3$ solution for 5 days (a, c) or for 3 days (b, d). The yellow circles in (d) show pre-existing defects.

Chapter 3

Methods

The goal of this work is the atomic-bond analysis of electron beam damage in hBN. This, of course, requires a tool that can make atoms visible. A microscope is an optical instrument used for observing small objects. It produces magnified images of the specimen.
The smallest distance between two points that we can resolve with our eyes is about 0.1–0.2 mm, depending on how good our eyes are, and assuming that there's sufficient illumination [28]. The concept of magnification has long been known. Basic optical microscopes can be very simple, although there are also many complex designs that aim to improve resolution and sample contrast. The microscope familiar to most people is a light microscope ($\sim$ 200 nm) with hundreds or thousands of times magnification of the specimen. But a limit will be reached very quickly. Because of the limited image resolution in those light microscopes, which is imposed by the wavelength of visible light, electron microscopes were developed.

3.1 Scanning Transmission Electron Microscopy (STEM)

This section is adapted from References [28, 29, 30].

A major attraction to the early developers of the transmission electron microscope was that, since electrons are smaller than atoms, it should be possible, at least theoretically, to build a microscope that could 'see' detail below the atomic level. But it turns out that its not that simple and many limitations and parameters have to be considered.

Because of diffraction and interference, absolute focus with particles with wave-like properties is not possible. Therefore, there exists a limit for the resolving power or resolution of a microscope

[31], the so called 'resolution limit'. A point of light cannot be focused perfectly into a point. Instead it forms concentric rings which are called an 'Airy disc'. A mathematical description of the resolution in a perfect optical system is given by the Abbe criterion. It states that the smallest distance that can be resolved, is given approximately by

$$\delta = 1.22\frac{\tilde{\lambda}}{2n\sin\beta} = 0.61\frac{\tilde{\lambda}}{n\sin\beta} = 0.61\frac{\tilde{\lambda}}{\mathsf{NA}}, \tag{3.1}$$

where $\tilde{\lambda}$ is the wavelength of the radiation, n the refractive index of the viewing medium, and β the semi-angle of collection of the magnifying lens. Abbe was also the first person who defined the term *numerical aperture* (NA) which is defined as $\mathsf{NA} = n\sin\beta$.

A slight modification of Abbe's equation was done by Rayleigh, resulting the Rayleigh criterion (equation 3.2)

$$\theta = 1.22\frac{\tilde{\lambda}}{D}, \tag{3.2}$$

where θ is the angular resolution and D the diameter of the lens aperture.The resolution limit defined by Rayleigh can be explained by the overlapping diffraction patterns of two airy discs.

In contrast to the light microscope, which uses light that is focused by glass or optical lenses, electron microscopes use electrons for imaging. Therefore, 'lenses' in an electron microscope are not glass lenses but magnetic lenses, which guide the electrically charged electrons through magnetic fields and form a focused electron probe. Therefore the wavelength of the electrons also need to be adapted relativistically, because they reach a considerable function of the speed of light. The relativistic wavelength λ_{rel} of the electron is given by

$$\lambda_{\mathsf{rel}} = 2\pi\hbar\left(2m_e eU\left[1+\frac{eU}{2m_e c^2}\right]\right)^{-\frac{1}{2}}. \tag{3.3}$$

With U the acceleration voltage of the microscope. The elementary charge is denoted by e, m_e is the rest mass of the electron, $\hbar$ is the reduced Planck constant with $\hbar = h/2\pi$ where h is the Plack constant and c the speed of light in vacuum.

Aside from the resolution criterion, the information which can be extracted by an electron microscope depends on some more parameters. One is the energy spread of the electron beam which leads to chromatic abberations and will be explained later. The composition, stability and

thickness of the specimen also plays a role, as was mentioned already.

From the beginning of the electron microscopy era until today many models have been constructed. Although we can roughly classify them into the transmission electron microscopy (TEM), the scanning transmission electron microscopy, scanning electron microscopy (SEM) and scanning transmission microscopy (STM).

The conventional TEM is a wide-beam technique, in which a close-to-parallel electron beam floods the area of interest and the image is formed by an imaging (objective) lens after transmission from the thin specimen.

For STEM, an electron probe is located in the back focal plane of the objective lens' pre-field and, similar to TEM, the electron probe represents a demagnified image of the electron source. This image is not perfect. There is an aperture present which limits the angular range of the illuminating electrons that form the electron probe.

The pioneering work of Albert V. Crewe (1966) [32] marks the beginning of practical scanning transmission electron microscopy. From then on, the scanning probe mode was developed as a complementary technique to the broad-beam illumination mode.

STEM deploys a fine focused beam, formed by a probe forming lens before the thin specimen, to adress each pixel in *series* as the probe is scanned across the specimen. So the formation of the electron probe is a central point of imaging with a STEM.

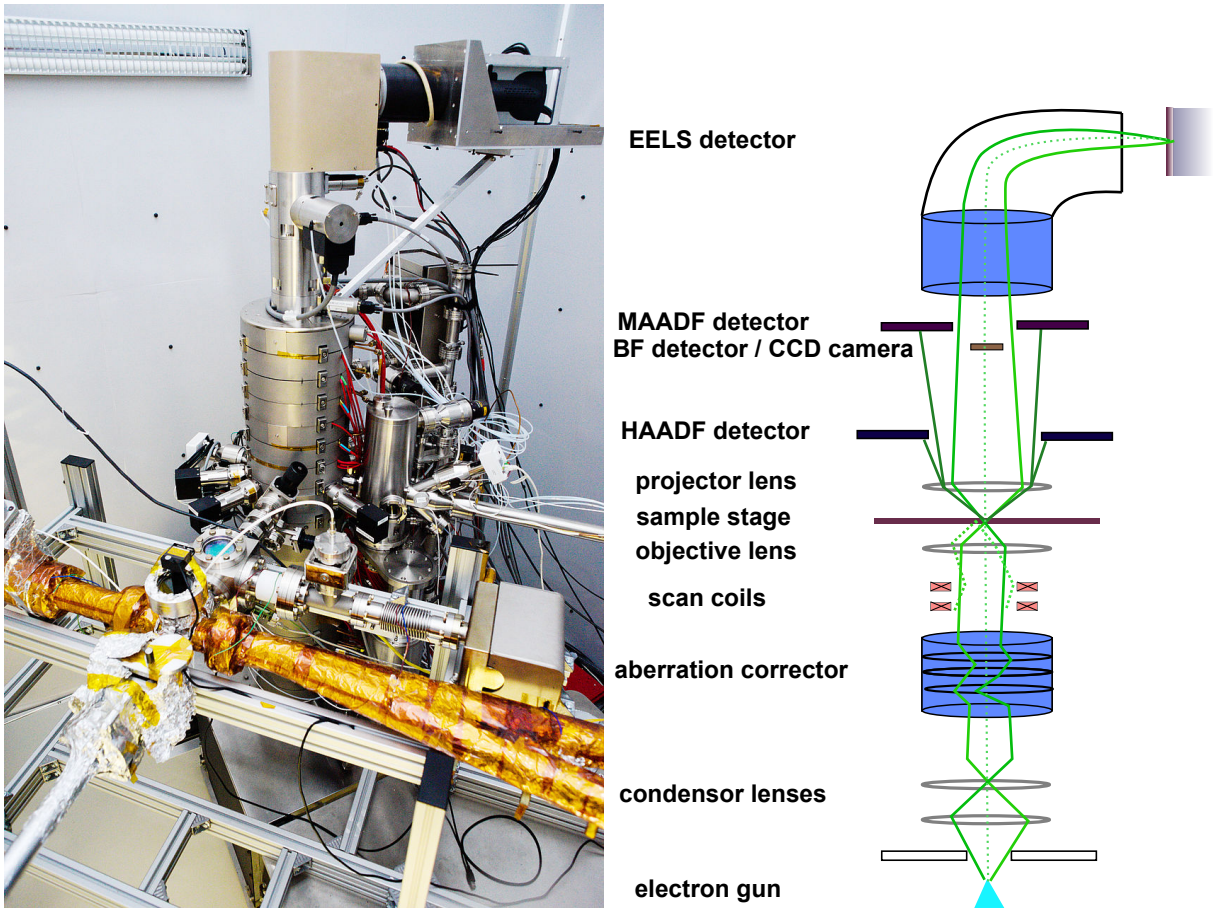

Figure 3.1: **A STEM instrument.** (left) The Vienna Nion UltraSTEM100. (right) A simplified schematic of a scanning transimisson electron microscope with paths of electron rays through the instrument. Figure is adapted with permission from Reference [33].

Figure 3.1 shows the Vienna Nion UltraSTEM100 at Sternwarte park and a simplified schematic of the electron path in STEM.

There are basically two kinds of electron sources. One is called a thermionic source, which produces electrons by heating. The other type is a cold field-emission gun (CFEG) as the source, which produces electrons when a large electric potential is applied between a cathode and an anode. Latter one is used in STEM. Vacuum is important to avoid contaminants building up on the tip. Even in ultra high vacuum (UHV) conditions this can happen, because even in a vacuum of 10^{-8} Pa, one monolayer of contaminants will form on a substrate in about seven hours [28].

Electrons are charged particles, and thus spiral through the lens field with a helical trajectory. Which means that for electrons with a higher energy, stronger lenses are needed due to larger magnetic fields to get similar ray paths.

3.1.1 Aberrations

Before we can start imaging we need to get atomic resolution of our specimen which is in our case hBN. Even though there are already many autocorrectors in the nionswift software there is still some manual tuning needed. Especially residual aberrations like astigmatism, coma and threefold astig can affect the atomic resolution, which could make it hard to interpret their contrast of individual atoms.

Spherical and chromatic aberrations impact the braod-beam phase-contrast imaging mode (i.e. in TEM) as well as the formation of the electron probe in scanning probe mode (i.e. in STEM). Aberrations basically describe the deviations from the optical behaviour of an ideal instrument, which provides an ideal image with the imaging characteristics of the Gaussian optics. The Gaussian optics enables the conceptual description of the term 'aberration'. An electron ray is described by two geometrical ray parameters. One is the complex corrdinate in the aperture plane $\omega = \theta_x + i\theta_y$ and the other one is the object plane $w_o = x_o + iy_o$. Knowing ω and w_o, the Gaussian optics can be applied to derive the position of a ray in the Gaussian image plane. The Gaussian image point in the Gaussian image plane is given by $w_i = x_i + iy_i$.

The spherical aberrations C_3 and the defocus C_1 cause a modulation of the phase of the electron wave in the aparture plane. The aberration function depends on the illumination angle of a particular electron trajectory in STEM and can be written as

$$\chi(\theta) = \frac{1}{2}\theta^2 C_1 + \frac{1}{4}\theta^4 C_3. \tag{3.4}$$

Employing the notation of the complex angle ω for the angle θ

$$\chi(\omega) = \frac{1}{2}\omega\bar{\omega} C_1 + \frac{1}{4}(\omega\bar{\omega})^2 C_3, \tag{3.5}$$

where $\bar{\omega}$ is the complex conjugate of ω. Defocus C_1, sperical aberration C_3 and chromatic aberration C_C are aparture or axial aberrations, which means, that they are only dependent on position coordinate in the aparture plane.

If we only had to consider the diffraction limit, we would simply employ the largest illumination aperture in order to obtain the smallest probe. However, the next contribution that needs our attention is the effect induced by the phase shifts caused by lens aberrations, namely by the

third-order spherical aberration C_3, whose effect can be balanced by proper choice of the defocus C_1.

Spherical and chromatic aberration are three major defects in electromagnetic lenses.

a) Spherical aberration

The disc of radius

$$\delta_S = \frac{1}{4} C_3 \alpha^3 \tag{3.6}$$

is called the *disc of least confusion*. It expresses the limitation imposed by the spherical aberration C_3 on achievable probe size for a given probe illumination semi-angle α. The smaller the illumination semi-angle, the smaller is δ_S.

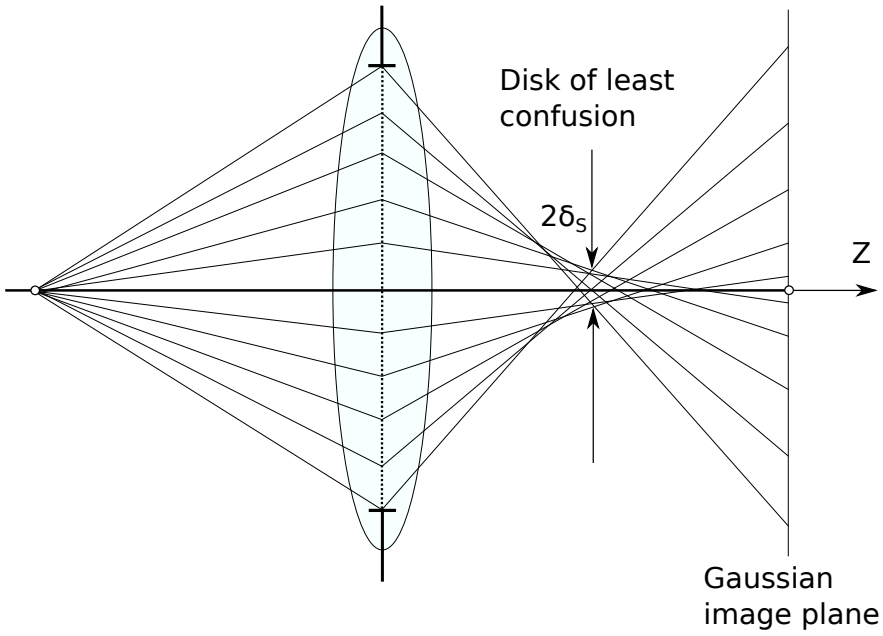

Figure 3.2: **Spherical aberration.** The disc of least confusion. Figure by the author, after Ref. [29].

b) Chromatic aberration

An ideal electron source emits electrons of equal energy. However, real electron sources emit electrons of slightly varying energy and thus exhibit a characteristic energy distribution. So chromatic aberration is related to the frequency, wavelength or energy of the electrons.

In general, the radius of the disc of confusion δ_C due to the chromatic aberration is given

by

$$\delta_C = C_C \alpha \frac{\Delta E}{E_0}, \tag{3.7}$$

where C_C is the constant of chromatic aberration of the lens and ΔE is a measure for the width of the energy distribution.

Hence, it is the spread of focus induced by the finite energy spread of the beam and the chromatic aberration which needs to be incorporated in the probe calculation.

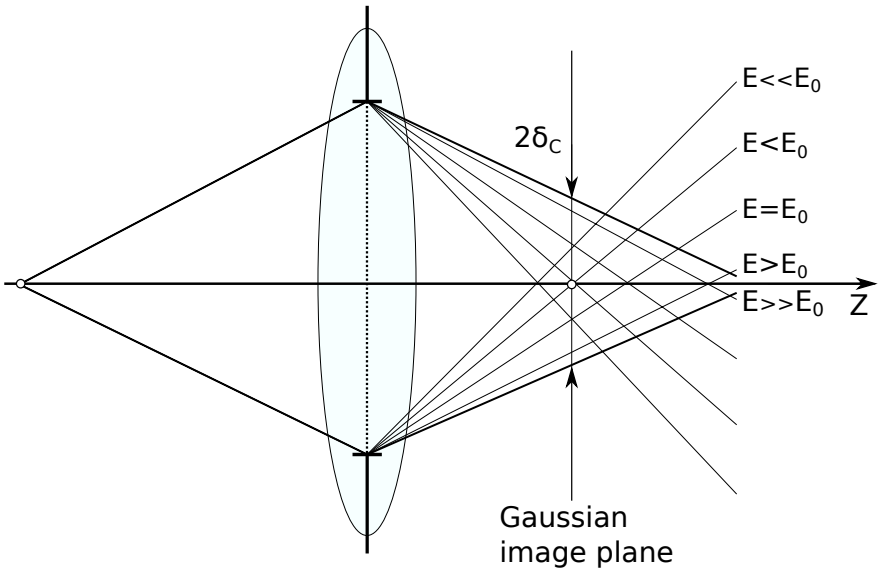

Figure 3.3: **Chromatic aberration.** The disc of confusion. Figure by the author, after Ref. [29].

3.1.2 Imaging

To optimize the resolution in STEM imaging, finding an optical setting with minimal effect of the probe-limiting factors such as sources and aberrations (section 3.1.1) is necessary. The resolution in STEM imaging is fundamentally limited by the size of the electron probe. Two objects which are at a distance smaller than the size of the electron probe cannot be resolved. The task of optimizing the resolution of a scanning transmission electron microscope means finding an optical setting for which the overall effect of the probe-limiting factors discussed above is minimal.

To form an image, the electron probe is raster scanned pixel by pixel through the specimen. On each scan position, the electron probe is propagating through the specimen. Each scan position produces a diffraction pattern, because electrons scatter from the atomic nuclei in the specimen.

While scanning the focused electron beam across the specimen, only a certain part of intensity of the diffraction pattern is recorded as a function of the beam position. The choice of the area of the diffraction pattern that is positioned on the detector determines the image contrast. For the forward scattered electrons a brightht-field (BF) detector can be used. Alternativley, an annular dark field detector can also be used for detecting scattered electrons by the atomic nuclei of the specimen.

ADF detectors collects the electrons scattered in a specific angular range using a ring-like detector and unscattered electrons pass through the hole in the middle part of the geometry, as shown in Fig. 3.1. To collect the electrons which are scattered at high angles with respect to the optical axis, a high angle annular dark field detector (HAADF) is used. Due to its incoherent nature, it also eliminate the diffraction contrast and allows the imaging of even heavier atoms. Electrons which are scattered at low to medium angles are detected using medium annular dark field detectors (MAADF). To image the lighter elements, it can be preferred as higher contrast comes from the collection of scattered electrons at lower angles.

Imaging of a single atom by using such a detector where the intensity of scattering follows the Rutherford scattering model. In this model the atomic number Z of the illuminated atom is proportional to Z^2. Experiments showed that the exponent value is around 1.6-1.8 instead of the theoretical approximation of 2 [34]. With ADF detectors images were taken with 'Z-contrast imaging' [35]. Thus, ADF imaging is very sensitive to the atomic columns and can be interepreted dirtecty from the intensity of individual atoms. It can be also used to identify the chemical nature of individual elements. [36]. According to this Z dependence atoms with higher atomic number appear brighter in a STEM image than lighter ones. In case of hBN, N atoms ($Z = 7$) will be slightly brighter than B atoms ($Z = 5$). The right panel of the Fig. 3.4 shows the atomic lattice of monolayer hBN. Blue cirlce with a brighter contrast shows a nitrigen atom and the boron atom is cirled in violet.

One of the relevant setup parameters for the Nion UltraSTEM100 [18] is the energy spread of the CFEG, which is 0.3 eV. The angular range with half angles for the MAADF mode is 40-60 mrad and for the HAADF mode is 80-240 mrad, are typical operating modes of the detectors. The convergence semi-angle is approximately 55 mrad.

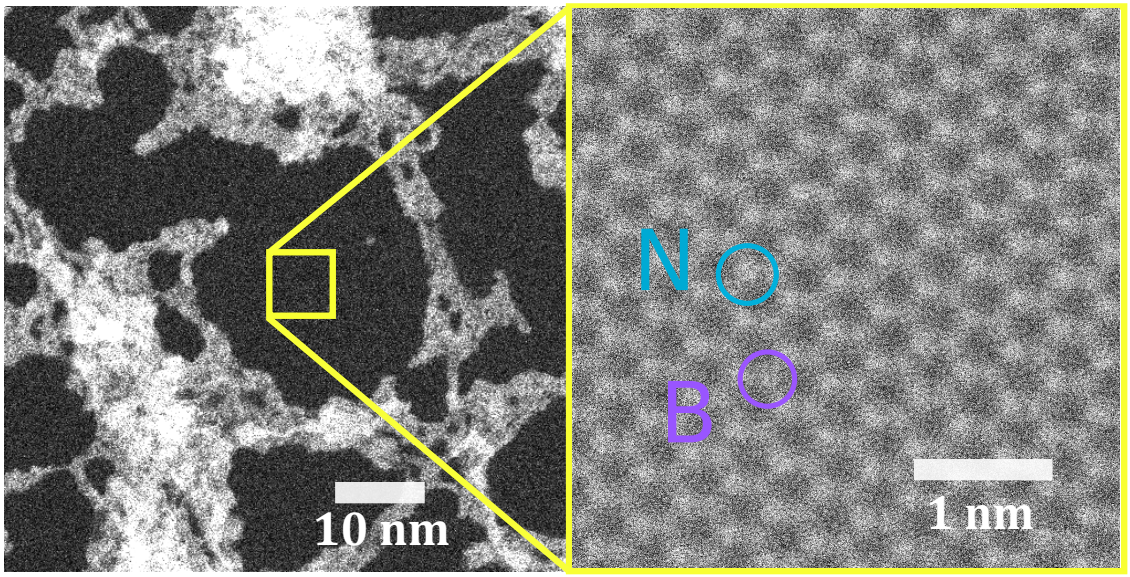

Figure 3.4: **STEM MAADF image of monolayer hBN.** The brighter contrast represents contamination. The zoomed in image shows the hexagonal atomic structure of hBN. Due to Z contrast imaging, N appear slightly brigther than the B.

3.2 Electron-irradiation damage

The electron beam used in an electron microscope (STEM, TEM, SEM etc.) can cause changes in the surface or bulk structure of a specimen. Damage caused by the electron beam can be explained with three main mechanisms. Figure 3.3 shows an illustration of this classification.

The first damage mechanism is knock-on damage, which is caused by (quasi-)elastic scattering. Thereby the electron transfers momentum to an atomic nucleus. Maximum energy transfer occurs when the electron backscatters at an angle of $180°$.

Inelastic scattering causes the second damage mechanism which is called radiolysis or ionization damage. Here the electron interacts with the electrons from the outer shell of the atom. This process is quite complex and still not well understood [37].

Gas atoms can also cause damage to the specimen due to beam-induced chemical-etching. The electron beam dissociates gas molecules, which can trigger chemical reactions.

In this work, we will focus mainly on the first two damage mechanisms because our experiments were conducted under ultrahigh vacuum (UHV) and no chemical-etching effects were to be expected [38].

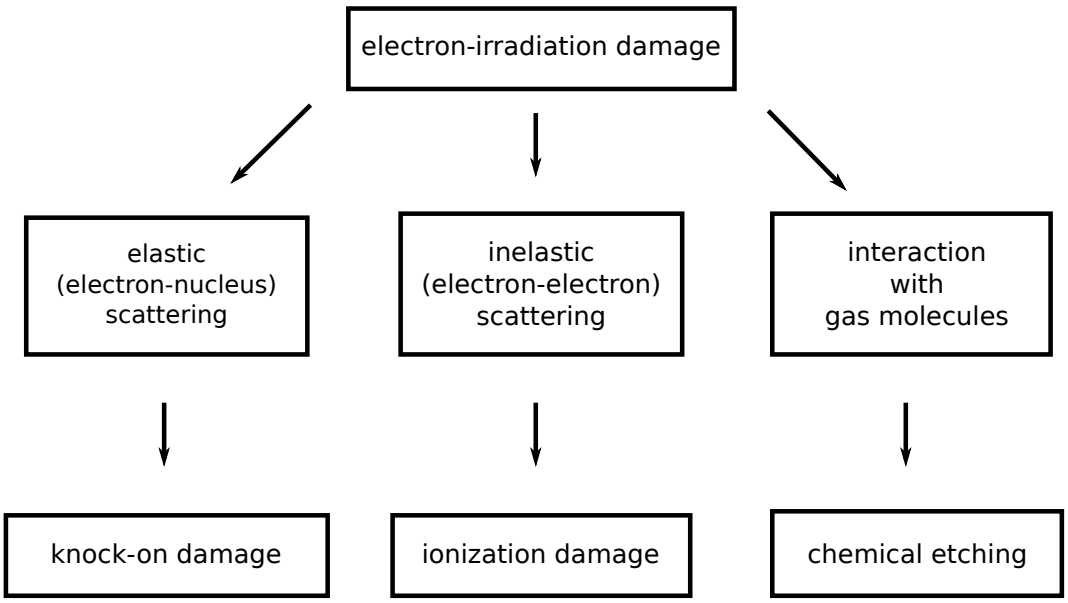

Figure 3.5: **Classification of radiation damage according to the type of electron scattering and interaction with gas molecules.**

3.2.1 (Displacement) Cross section

Cross section σ describes the probability of scattering. Detailed calculations and descriptions of the relations of the scattered electrons through an angle θ and the total solid angle of scattering is Ω, which are illustrated in Fig. 3.5, can be found in [28]. A short description of the total cross section will be provided in this section.

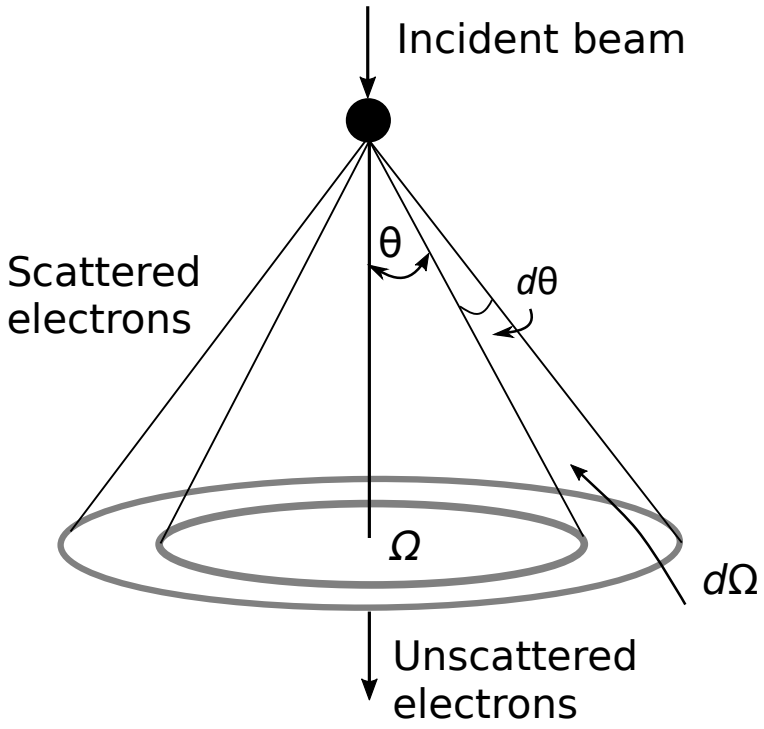

Figure 3.6: **Electron scattering by a single isolated atom.** Electrons are scattered through an angle θ and the total solid angle of scattering is Ω. An incremental increase in scattering angle $d\theta$ gives an incremantal increase in a solid angle $d\Omega$, which is the basis for determining the differential scattering cross section. Figure by the author, after Ref. [28].

Differential cross section $(d\sigma/d\Omega)$ describes the angular distribution of scattering from an atom

$$\frac{d\sigma}{d\Omega} = \frac{1}{2\pi \sin\theta} \frac{d\sigma}{d\theta}, \tag{3.8}$$

where by integrating equation 3.6 from 0 to θ we will get the scattering cross section σ_{atom} for the simple case with one atom. θ is a scattering semi-angle of the scattered electron. As shown in Fig. 3.6 electrons are scatteres through an angle θ into a solid angle Ω.

$$\sigma_{\text{atom}} = \int_0^\theta d\sigma = 2\pi \int_0^\theta \frac{d\sigma}{d\Omega} \sin\theta d\theta \tag{3.9}$$

An expansion for a more real case with N atoms instead of a single isolated atom we can define the total cross sections for scattering from the specimen (in units of m^{-1}) as

$$\sigma_{\text{total}} = N\sigma_{\text{atom}} = \frac{N_A \sigma_{\text{atom}} \rho}{A} \tag{3.10}$$

With this we got a very simple description of the total cross section with N_A the Avogadro's number and A is the atomic weight of the scattering atoms in the specimen (kg mol^{-1}) which has density ρ (kg m^{-3}).

Expressions for the cross section become more complicated by trying to give better approximations for the scattering in real specimen. Formulas for the cross sections need to be modified, as we'll see in the next two sections. However, the more complex equations don't alter the basic scattering behaviour predicted by the simple equations.

3.2.2 Elastic scattering

Elastic scattering represents electrostatic deflection of incoming electrons by the Coulomb field of each atomic nucleus. Elastic means in this case that the sum of the kinetic energies is conserved in the scattering process. It gives rise to electron-diffraction patterns and to diffraction and phase contrast in TEM images, as well as backscattered-electron (BSE) contrast in SEM images and to Z-contrast in STEM. In some circumstances it can also result in atomic displacements within a crystalline specimen, or electron-beam sputtering of atoms from its surface.

Displacement threshold energy T_d is the minimum amount of kinetic energy that is needed by a nucleus to be knocked out from its lattice site. In comparison to the threshold energy, the cohersive energy and the defect formation energy are potential energies. The cohersive energy is the energy needed to rip the chemical bondings of a sample apart into widely separated atoms. The defect formation energy is the difference between the values for the ideal crystal and for the defective one. By combining a microscopic picture of the production and evolution of defects in hBN and computer simulations with HR-TEM experiments on electron irradiation of hBN, Kotakoski et al. [11] calculated the knock-on displacement threshold for boron and nitrogen atoms in the pristine structure and at different vacancy edges in various charge states. With density-functional theory calculations they obtained for pristine structures $T_d^B = 19.36$ eV and $T_d^N = 23.06$ eV for boron and nitrogen, respectively. Here only the ground-state dynamics were considered. The beam-induced excitation may reduce the bonding energy of the atoms in the lattice, thus reducing the threshold energy.

From T_d, one can estimate the displacement cross section σ under known electron-beam conditions using the McKinley-Feshbach formalism for Coulombic scattering of relativistic electrons, as described in Reference [39].

To describe the energy transfer of a scattering process, relativistic energy-momentum conservation has to be considered. The energy transfer equations for an elastic scattering between an eletron and atomic nucleus are described in Reference [14]. Beside the general case,

$$E(E,\theta,v) = \frac{2\left(E\left(E+2m_ec^2\right)\right) + \sqrt{E\left(E+2m_ec^2\right)}Mvc\left(1-\cos\theta\right) + \left(Mvc\right)^2}{2Mc^2} \tag{3.11}$$

which depends on the electron scattering angle θ, the kinetic energy E of an electron and the rest mass m_e from an atomic nucleus with mass M at velocity v parallel to the beam, two illustrative limits were calculated and described. First limit

$$E(E,\theta,v=0) = \frac{E\left(2m_ec^2\right)}{Mc^2}\left(1-\cos\theta\right) = \frac{2E\left(E+2m_ec^2\right)}{Mc^2}\sin^2\frac{\theta}{2} \tag{3.12}$$

describes the nucleus at rest, which means the velocity is zero ($v=0$).

For the second limit a backscattering of the electron is considered ($\theta = 180°$).

$$E_{\mathsf{max}}(E,\theta=180°,v) = \frac{\left(2\sqrt{E\left(E+2m_ec^2\right)}+Mvc\right)^2}{2Mc^2}. \tag{3.13}$$

For the latter case, the maximum energy transfer can be recovered. The energy of the electrons correspond exactly to the acceleration voltage. Considering only the static nucleus ($v=0$) an back-scattering ($\theta = 180°$, in hBN for example electrons with an energy of 60 keV or 80 keV can transfer a maximum energy of 12.87 eV or 17.48 eV to B and 9.93 eV or 13.49 eV to N.

As mentioned in section 3.2.1 the total cross section needs to be modified for more complex scattering cases. Back in 1948 McKinley and Feshbach [39] obtained a displacement cross section for the Coulomb scattering of relativistic electrons by atomic nuclei, using theoretical formulas obtained by Mott [40]. Displacement cross section can be used for quantifying damage occuring in the sample, that happens when the transferred energy is greater than T_d. The formula for the elastic scattering case is [14, 13, 17]

$$\begin{aligned}\sigma_{\mathsf{KO}}(E,v) = 4\pi\left(\frac{Ze^2}{4\pi\epsilon_0 2\gamma m_0c^2\beta^2}\right)^2\Bigg[\left(\frac{E_{\mathsf{max}}}{T_d}-1\right) - \\ \beta^2\ln\left(\frac{E_{\mathsf{max}}}{T_d}\right) + \pi Z\alpha\beta\left\{2\left(\sqrt{\frac{E_{\mathsf{max}}}{T_d}}-1\right) - \ln\left(\frac{E_{\mathsf{max}}}{T_d}\right)\right\}\Bigg].\end{aligned} \tag{3.14}$$

Here E_{max} is the maximal transferred energy as described in equation 3.11. ϵ_0 is the dielectric constant. The relativistic factor for the electron is $\beta(E) = \sqrt{1-(1+E/m_e c^2)^{-2}}$ with a corresponding Lorentz factor $\gamma = 1/\sqrt{1-\beta^2}$, $\beta = v/c$ and α is the fine structure constant $\alpha = Z/137$ with Z as the atomic number.

3.2.3 Inelastic scatterring

Inelastic scattering represents Coulomb interaction of incoming electrons with the atomic electrons that surround each nucleus. The scattering angle is lower than for the elastic scattering case ($\sigma \sim Z^2$) and it also gives rise to secondary-electron production [37]. This process leads to the emission of X-rays (used for elemental analysis in the STEM, TEM and SEM), provides SEM images and electron energy-loss spectra (EELS).

Inelastic scattering leads to a retardation and change in direction of the electron, as well as excitation or ionization of the target atoms. Considering those factors it is very challenging to build up a full theorical formalism of this mechanism. By using the Bethe formalism [41], and converting to SI units Susi et al. [14] got an approximation for the total radiolysis cross section

$$\sigma_{\text{rad}}(E) \approx 4\pi \frac{Ze^4}{(4\pi\epsilon_0)^2 2\gamma m_e c^2 T_d \beta^2} \left[\log\left(\frac{2\gamma m_e c^2 \beta^2}{T_d(1-\beta^2)}\right) - \beta^2\right] \zeta, \tag{3.15}$$

where ζ is an efficiency factor (which includes the contribution of shell-dependent factors) describing the proportion of ionization events.

So far experiments were theoretically compared for knock-on mechanism [17]. For materials which are semiconducting or insulating like MoS_2 and hBN, a separate comparison by fitting the theoretical formulas as described earlier with (S)TEM experiments seems not accurate. A first try by Kretschmer et al. [15] to combine both mechanisms looks promising. The total cross section $\sigma^{\text{tot}}(E)$ for the combined case is a sum of the cross sections for the knock-on events for the ground $\sigma(E, T_d^{\text{gs}})$ and excited $\sigma(E, T_d^{\text{exc}})$ states scaled by the probability $\sigma_{rad}(E)$ from equation 3.13:

$$\sigma_{\text{tot}}(E) = \sigma(E, T_d^{\text{gs}}) + \sigma(E, T_d^{\text{exc}}) \times \sigma_{\text{rad}}(E). \tag{3.16}$$

So the displacement cross section with the electronic excitations is determined as

$$\sigma_{\text{exc}} = \sigma\left(E, T_d^{\text{exc}}\right) \times \sigma_{\text{rad}}\left(E\right). \tag{3.17}$$

They showed their results by comparing the theory with HRTEM experimental data of MoS_2 in Fig. 3.7. The blue solid line shows the ground state for a knock-on event with a threshold energy of $T_d = 6.5$ eV. The excited state is shown with the red solid line. The green solid line is the radiolysis cross section with $\sigma_{rad}(E) \sim 1/E$. The orange solid line is the most accurate fit with the total cross section to the experimental TEM data points with $T_d = 1.5$ eV. To show the effect of the T_d, the orange dashed line shows also the total cross section but with a higher threshold energy of $T_d = 3.5$ eV corresponding to a simulated value. For the latter threshold energy, it is clear that the curve doesn't match the experiental data points.

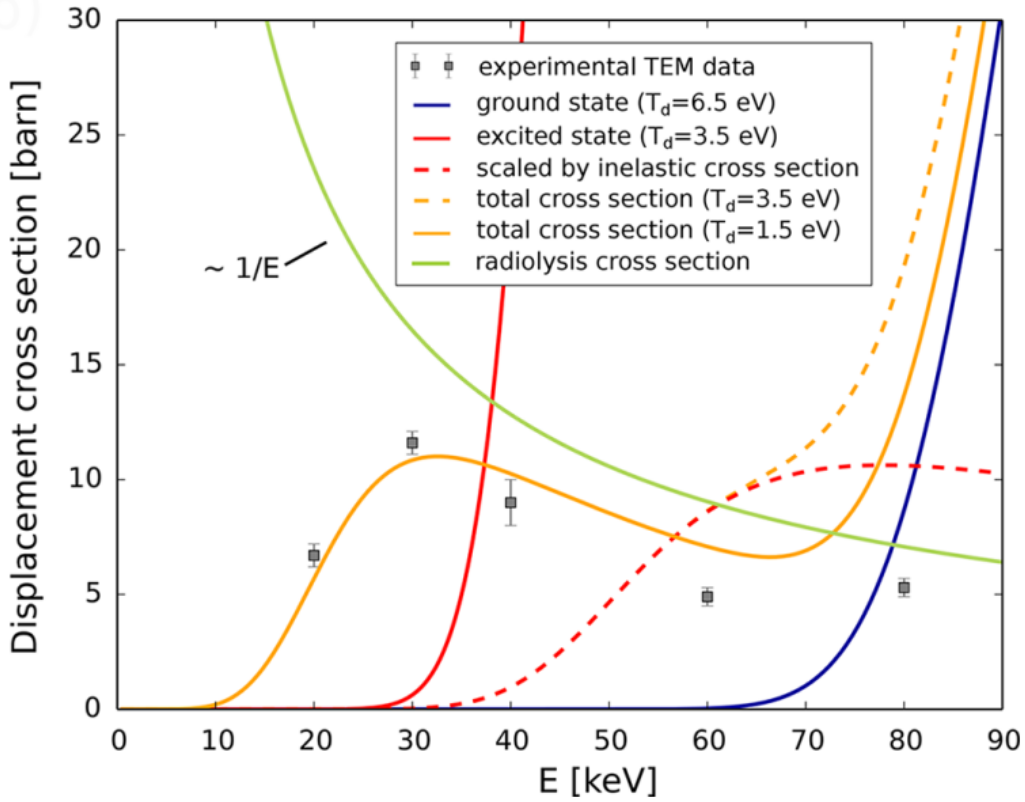

Figure 3.7: **Displacement cross section for MoS_2.** The experimental (squares) and theoretical (curves) displacement cross sections of S atoms in MoS_2. Figure is adapted with permission from [15], Copyright 2020 (American Chemical Society)

Chapter 4

Results and Discussion

Before we turn on the electron beam we should be aware of which acceleration voltage we want to work with, because the microscope needs some time to stabilize for further work. So an optimal workday is choosing one acceleration voltage for the day to work with. Is the energy too high the hBN structure will be damaged too fast, which will be explained in the next section. Is the energy too low it can be that there is no damage at all and we don't see any defects which is useless for our work as we wanted to observe and analyse the damage mechanism. Another aspect which needs to be considered is that the setup in the microscope needs to be aligned for each acceleration voltage to achieve atomic resolution. In our case we used 55 kV, 60 kV, 70 kV and 80 kV, because the damage creation rate is low enough for hBN.

To avoid a so called 'dose-rate-effect' [42], we have to be consistent with our scanning setups which includes the dwell time and the pixels per frame. With this effect we can get the same dose at different exposure times, which will lead to wrong statements. Dwell time is the time the beam spends in each pixel of the frame. Structural changes during the scan can be captured faster with a shorter dwell time but it will give a poorer contrast. We used a dwell time of 16μs. The higher the number of pixels the less blur and the better we can see the image due to high signal to noise ratio. But this will again slow down the scan. A reasonable number was 512×512 pixels per frame. Those values were used for all the sequences.

Of course we also can change the magnification in a microscope. We varied the field of view (FOV) to examine if there is any difference in the displacement cross section. An example is shown in Fig. 4.1 with 3 different FOVs (1.8 nm, 2.4 nm, 3.1 nm) for acceleration voltage of 80 kV. Because the electron flux is different at each FOV, a systematic study can give more detailed

information about dose rate effect on the displacement cross section. Our range of FOV was 1.9 - 3.1 nm.

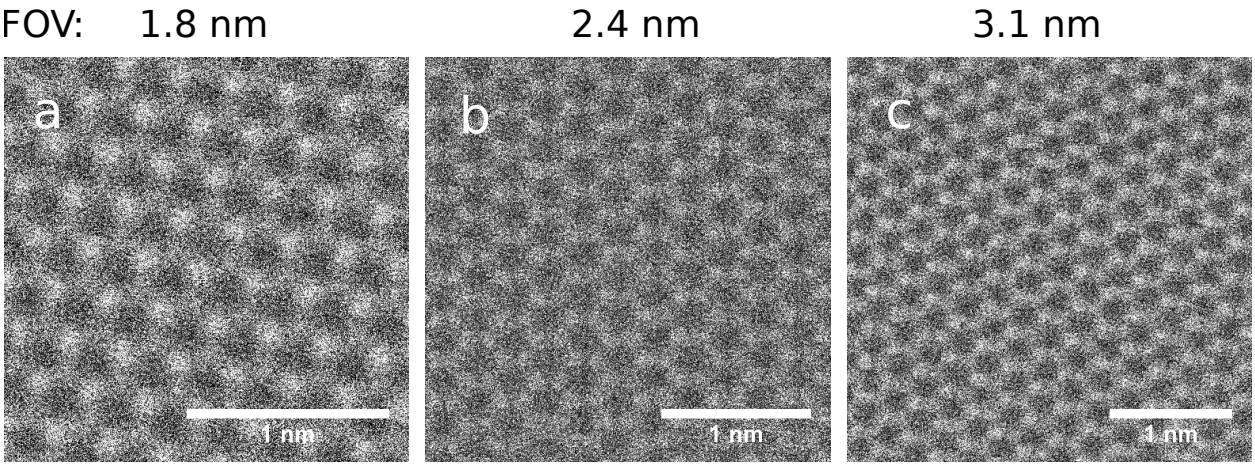

Figure 4.1: **MAADF-STEM images showing monolayer hBN atomic structures at different FOVs.** Image series were recorded at 80 kV acceleration voltage with MAADF detector.

4.1 Image analysis

After the microscope is tuned minimizing the aberrations for achieving atomic resolution, we can start recording our image sequences. For our initial state, we need a pristine area. Now we will leave the beam on this region and observe this area until the first defect occurs. For the data analysis we recorded image sequences. We are only interested in the first upcoming defect, so we stoped recording the image after the first defect occured.

We analysed images manually, because there is no reliable, automatized software available yet. We also take into the accounts to total number of frames before the first defect appears in the hBN structure. The way the microsope raster scans pixel by pixel in a line. So we define the position of our first defect by following the scanned line from top to bottom and from left to right. The chosen unit of this position is in pixel. So in one frame the pixel number of the n and m direction lies between 0 and 512. One example with is shown in Fig. 4.2. Fig. 4.2 a & 4.2 b are full frames without defect. One full frame has the total pixel number of $512 \times 512 = 262144$. Fig. 4.2 c is the first frame with a defect, therefore the pixel position can be determined with the poition m of the line n , added to the pixels of the n lines (i.e. $512 \times 200 + 240 = 102640$).

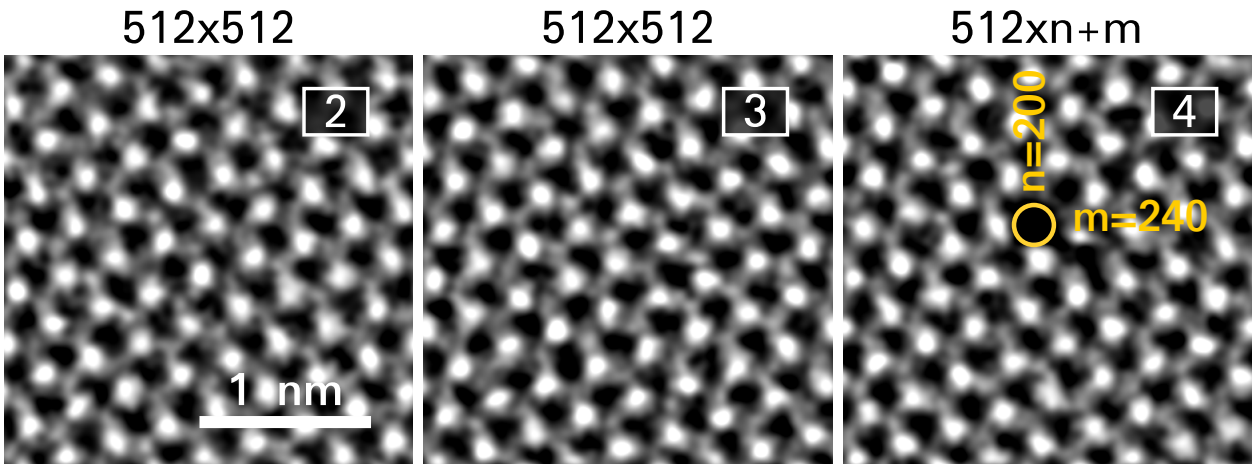

Figure 4.2: **MAADF-STEM images showing pixel position** Frame 2 & 3 shows images with 512x512 pixels per image without defect. Yellow circle in frame 3 shows the position in pixels (vertical position $n = 200$, horizontal position $m = 240$). Images were recorded at 70 kV and have been processed using the double Gaussian filter [36] ($\sigma 1 = 0.24$, $\sigma 2 = 0.15$, weight $= 0.30$).

The expected first defect is a single vacancy (one missing atom). More details about the various point defect configurations in 2D hBN can be found here [10]. In case of a single vacancy, the position of the defect can be identified when B or N atoms leave their positions. However, more than one B or N or both B and N vacancies may occur at the same time in the FOV. In this case the first defect in the image counts. Examples of defects are shown in Fig. 4.3 & 4.4.

4.1.1 Single vacancy

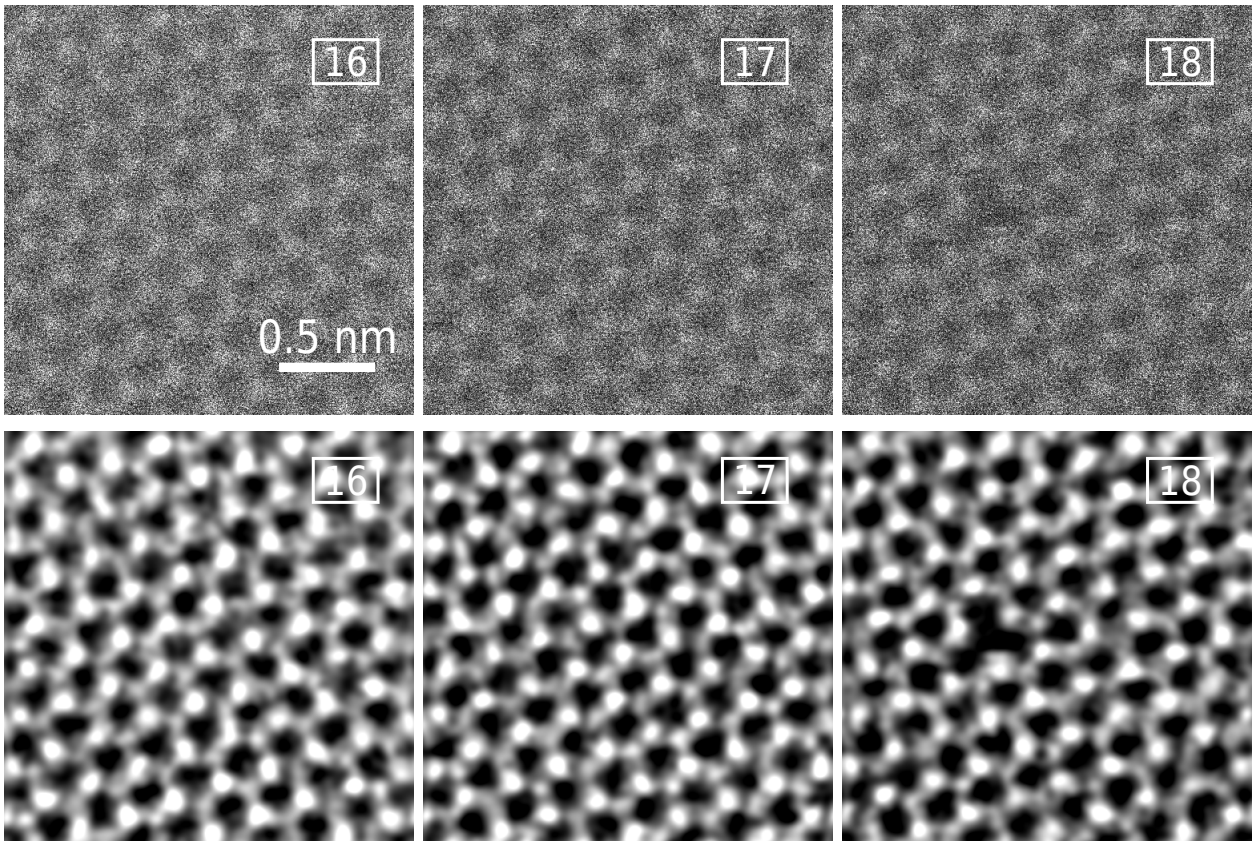

Figure 4.3: **MAADF-STEM images showing single B vacancy in monolayer hBN.** First two raw STEM images (first row) are from the image sequence before the defect appears. Frame 18 shows the first B vacancy. The overlaid numbers are the number of each image within the series. Images in the second row have been processed using the double Gaussian filter ($\sigma 1 =$ 0.23, $\sigma 2 =$ 0.15, weight $=$ 0.28).

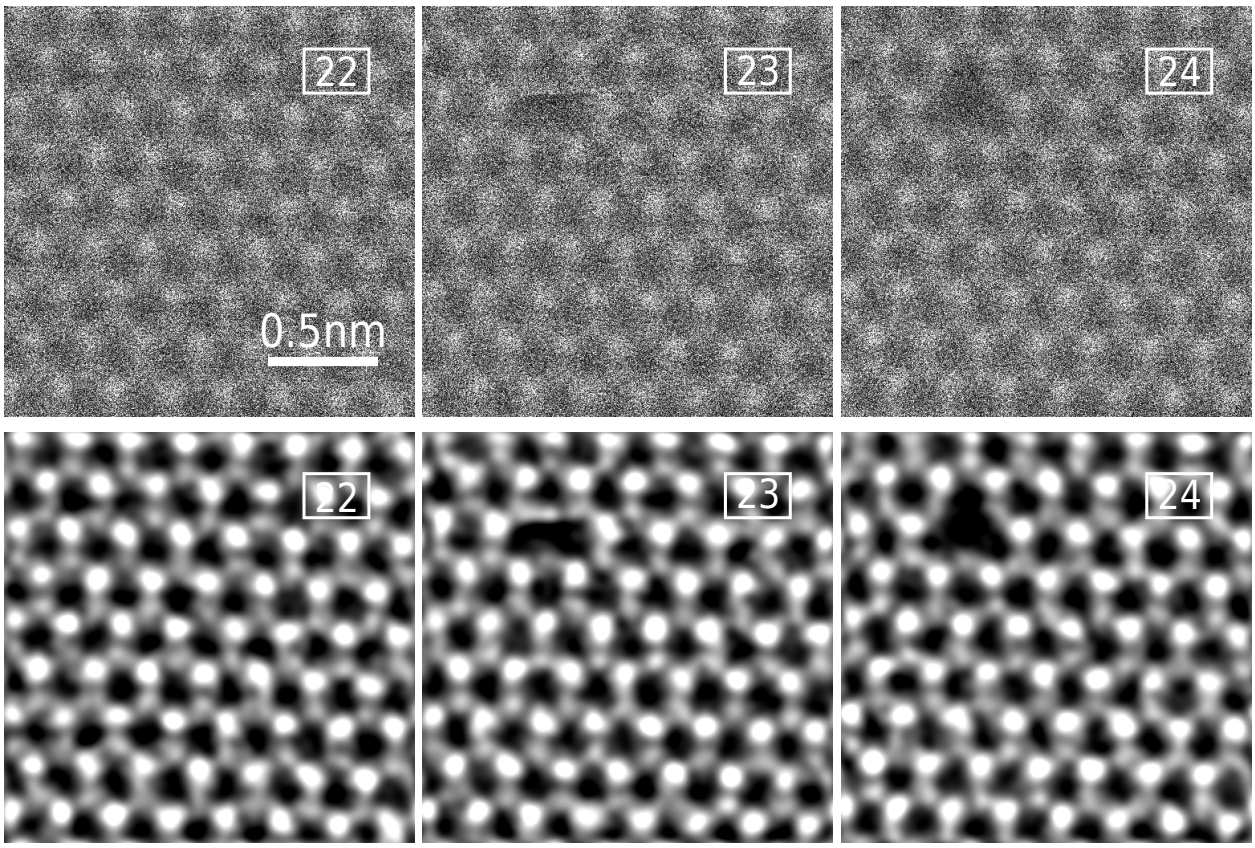

Figure 4.4: **MAADF-STEM images showing single N vacancy in monolayer hBN.** First two raw STEM images (first row) are from the image sequence before the defect appears. Frame 23 shows where N atom is not fully ejected and caught during scanning. Frame 24 shows the first N vancancy. The overlaid numbers are the number of each image in the series. Images in the second row have been processed using the double Gaussian filter ($\sigma 1 = 0.24$, $\sigma 2 = 0.16$, weight $= 0.29$).

The first row of Fig 4.3 are unfiltered raw images. The second row are double Gaussian filtered images [36]. In frame 16 and 17 the scanned area is pristine and has no defect. This changed in frame 18. One single boron atom is now missing from the structure.

Figure 4.4 demonstrates the same process but with the N atom in hBN. Here in frame 23 we managed to acquire an image a N atom was knock-out while scanning over it. Different to figure 4.3 one single nitrogen atom is kicked out leaving a single vacancy.

4.1.2 Other defects

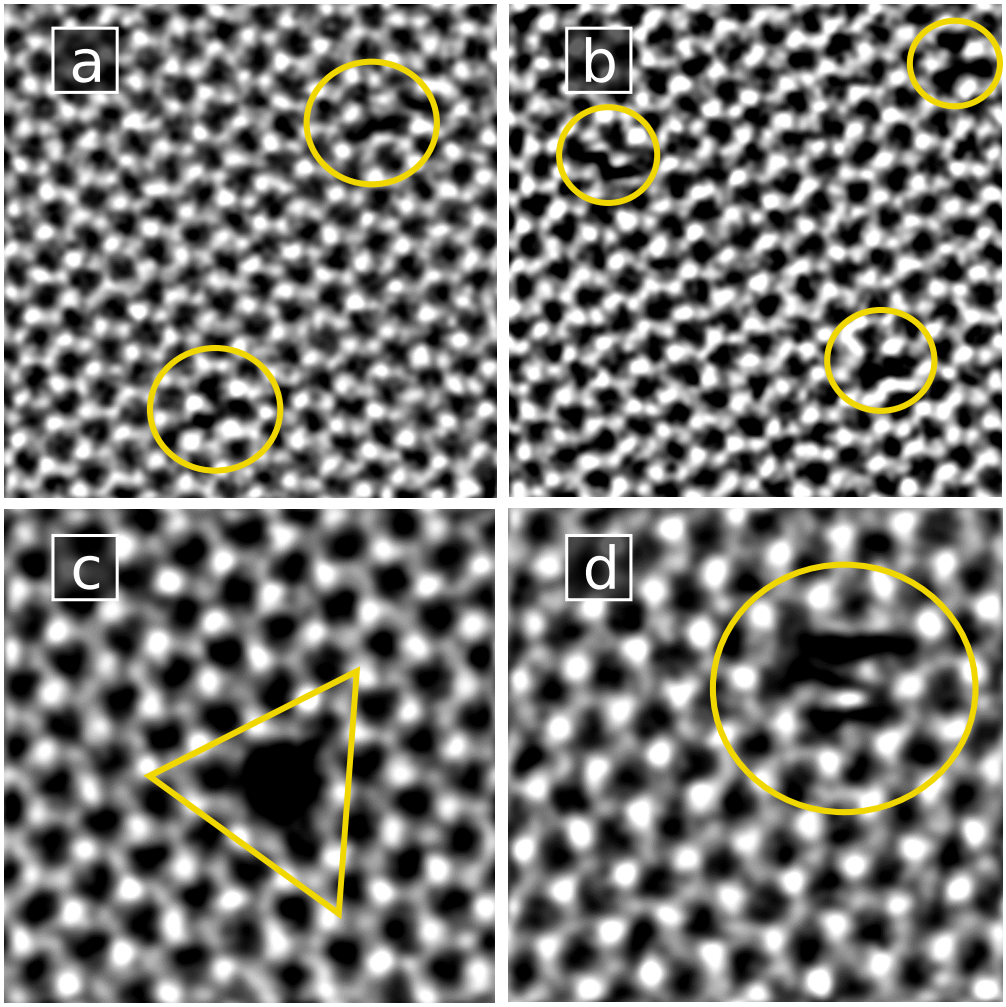

Figure 4.5: **STEM images showing other types of defects in hBN.** (a) Two single B vacancies. (b) Three single B vacancies. (c) Triangular shaped defect with three nitrogen and one boron atoms missing. (d) Defect with several B and N atoms missing. Due to dynamics it is not clear how many atoms are missing. Images have been processed using the double Gaussian filter ((a)-(b) $\sigma 1 = 0.25$, $\sigma 2 = 0.15$, weight $= 0.30$, (c) $\sigma 1 = 0.24$, $\sigma 2 = 0.14$, weight $= 0.29$, (d) $\sigma 1 = 0.22$, $\sigma 2 = 0.13$, weight $= 0.25$).

We observed not only single vacancies but also other types of defects, some of which are shown in Fig. 4.5. Two single B vacancies in the same frame are shown in Fig. 4.5 a. Those two missing atoms are constantly from the same element, i.e. two boron or two nitrogen atoms but not one of each. In Fig. 4.5 b we have the same situation but with three missing B atoms.

Fig. 4.5 c shows a triangle-shaped hole with three nitrogen and one boron atom missing. Such triangle shaped defects were quite stable for many frames, before the hole grows bigger. Another

larger defect is shown in Fig. 4.5 d. Due to dynamics it is not clear how many atoms are missing.

4.1.3 Dose until first defect

The electron dose ϕ is defined as the number of the electrons hitting the specimen. The dose rate ϕ_R (s^{-1}) is defined by a beam current i on the sample divided by the elementary charge

$$\phi_R = \frac{i}{e} = \frac{I_{\text{VOA}} \times C}{e}. \tag{4.1}$$

In the experimental setup the current can not be measured directly on the sample. From the metadata we know the virtual objective aperture (VOA) current I_{VOA} and can calculate the current on the sample with a constant C.

The time t_d until the first defect occured is the total number of pixels multiplied by the dwell time t_{dwell}

$$t_d = P \times t_{\text{dwell}}. \tag{4.2}$$

With equations 4.1 and 4.2 we get the dose ϕ until the first defect

$$\phi = \phi_R \times t_d. \tag{4.3}$$

4.2 Statistical analysis

We assume that our experimental data follows a Poisson process and therefore the obtained doses follow the exponential distribution. The exponential distribution is used to describe processes which have continous and independent events at a constant average rate [43]. This is the case for a knock-on process. To illustrate if the data follows a Poisson process, histograms were plotted. Those histograms contain the event counts with respect to the dose. After verifying that the data is Poisson distributed, an exponential distribution is obtained by cumulating the doses in discrete bins. The first bin contains the total number of all events (counts). In the next bin only events with doses higher than the binwidth remain. The same procedure is repeated for the following bins until the last one.

This exponential fit-value is our expectation value λ for the dose for each set of experimental parameters. It is adapted from the probability density function

$$f(\phi) = \begin{cases} \lambda e^{-\lambda\phi} & \text{for } x \geq 0 \\ 0 & \text{else} \end{cases}, \tag{4.4}$$

where ϕ is the dependet dose parameter.

Because both boron and nitrogen atoms can be displaced, but they have different T_d, they must be analyzed separately. Correspondingly the doses until defect need to be added up separately for boron and nitrogen. Table 4.1 there is an example for the 70 kV acceleration voltage experiment with the first 30 doses. The numbers marked with a '*' indicate that a change in the element happened and the dose is summed up in the 'added dose' column. The summed up dose consists of all doses of one element and the first dose of the other element when the first switch happened. One example will be the summed up B dose in the 9th line, where the first change from N to B started, with a value of $0.16 \cdot 10^{10}$. To get this we added each dose from the second column starting from line 2 to 9.

4.3 Experimental determination of σ

For the calculation of the displacement cross section σ (equation 4.5) from the experimental data following parameters are needed. The first part is the expectation value λ of the dose as described in the previous section. The second part is the areal density ρ of hBN. Therefore the displacement cross section is the reciprocal value of the expectation value λ and the areal density ρ

$$\sigma = \frac{1}{\rho \times \lambda}. \tag{4.5}$$

The areal density is the surface packing density of a hexagon [44], which is 2 atoms divided by the area of a hexagon

$$\rho = \frac{2}{A_{\text{hexagon}}} = \frac{4}{\sqrt{3}a^2}, \tag{4.6}$$

where

Table 4.1: **Example of experimental sequence for the doses until B and N vacancies.**

Nr.	Dose (10^{10} e^-)	Added Dose (10^{10} e^-)	Element
1	0.040		B
2*	0.50	0.54	N
3	3.84		N
4	1.60		N
5	0.38		N
6	6.38		N
7	1.05		N
8	1.19		N
9*	1.49	16.4	B
10*	4.06	5.55	N
11	1.51		N
12	6.79		N
13	1.50		N
14	0.91		N
15*	0.088	14.9	B
16*	0.57	0.66	N
17	1.71		N
18	0.70		N
19	1.86		N
20	4.09		N
21*	1.09	10.0	B
22	1.06		B
23	1.86		B
24	2.80		B
25*	2.54	9.36	N
26	0.67		N
27	0.54		N
28	1.27		N
29	3.16		N
30*	1.73	9.89	B

$$A_{\text{hexagon}} = \frac{\sqrt{3}}{2}a^2 \tag{4.7}$$

with $a = 1.45$ Å.

The uncertainty of the experimental data was obtained by Gaussian error propagation.

The results of this work will be shown in this chapter. It is divided into two parts. The first part is the analysis of the experimental data and the second part is the comparison of them with theoretical predictions with respect to the radiolysis mechanism.

All experiments were done with the Nion UltraSTEM 100 in Vienna. The first part however are divided again into two subsections. In our analysis, we considered various parameters to get the accurate values for the electron doses and displacement cross sections. In particular, we used different acceleration voltages, recording image series at different FOVs to vary the electron fluences. Also, we observed the ejection of both B and N atoms as our first defect, thus we separated the number of cases of each elements.

4.4 Exponential fits of a Poisson process

4.4.1 σ for combined B & N electron doses with different FOVs

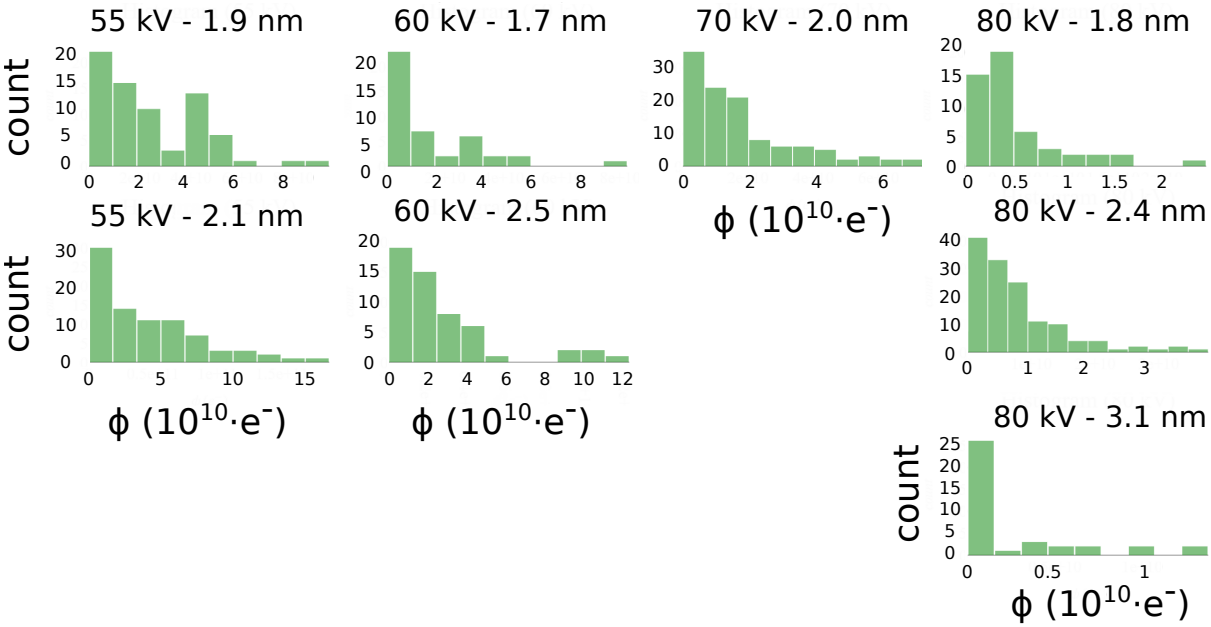

Figure 4.6: **Histograms of combined B & N electron doses.** Combined B & N electron doses until first displacement for different acceleration voltages $55 - 80$ kV with different field of views $1.7 - 3.1$ nm.

Fig. 4.6 shows histograms for the combined dose of B & N until the first defect at different FOVs and acceleration voltages. For 55 kV experiments, 1.9 nm and 2.1 nm FOV were used, for 60 kV we used 1.7 nm and 2.5 nm. For 70 kV experiments, only one FOV (2.0 nm) was used, and for 80 kV we have 1.8 nm, 2.4 nm and 3.1 nm. The counts of the calculated electron dose from the experimental data is collected within a suitable bin and is shown on the y-axis. With those histograms we show that the data is Poisson distributed. Except with the '55 kV - 1.9 nm' data this is the case. '55 kV - 1.9 nm' has an obvious peak in the middle. This could be explained with a radiolysis effect at low acceleration voltage as explained in Chapter 2.

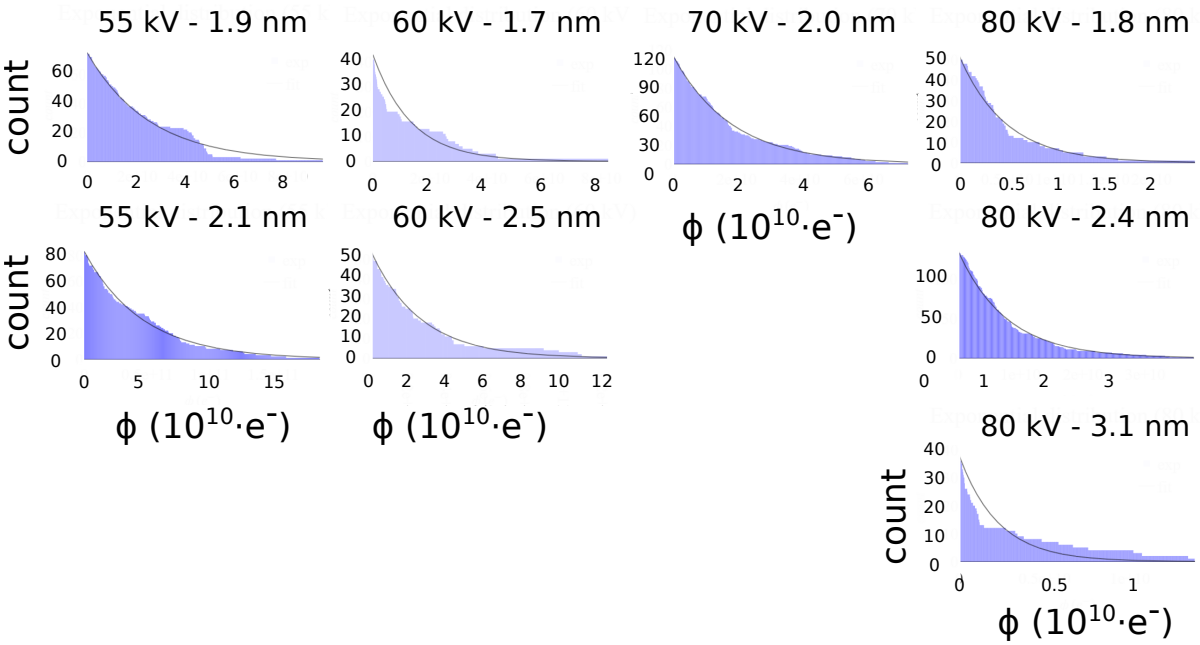

Figure 4.7: **Exponential distribution of combined B & N electron doses.** Exponential distribution with the expectation value λ as the fit (black solid line) for different acceleration voltages $55 - 80$ kV and different field of views (FOV) $1.7 - 3.1$ nm.

With the same datasets, exponential distributions were created and are shown in Fig. 4.7. The combined B & N doses were arranged cumulatively and the binwidth is for each plot the smallest dose value. The black solid line shows the exponential fit, which corresponds to the expectation value λ (equation 4.1) of the electron dose until defect. Those expectation values and their calculated errors are listed in table 4.2.

Table 4.2: **Expectation values λ for the combined B & N electron dose until first displacement.**

Acc. voltage (kV)	FOV (nm)	λ ($\times 10^{10} e^-$) of dose until defect	$\Delta\lambda$ ($\times 10^{10} e^-$)
55	1.9	2.50	$\pm$0.028
55	2.1	4.63	$\pm$0.026
60	1.7	1.34	$\pm$0.036
60	2.5	2.54	$\pm$0.027
70	2.0	1.84	$\pm$0.0074
80	1.8	0.48	$\pm$0.0054
80	2.4	0.78	$\pm$0.0036
80	3.1	0.23	$\pm$0.0092

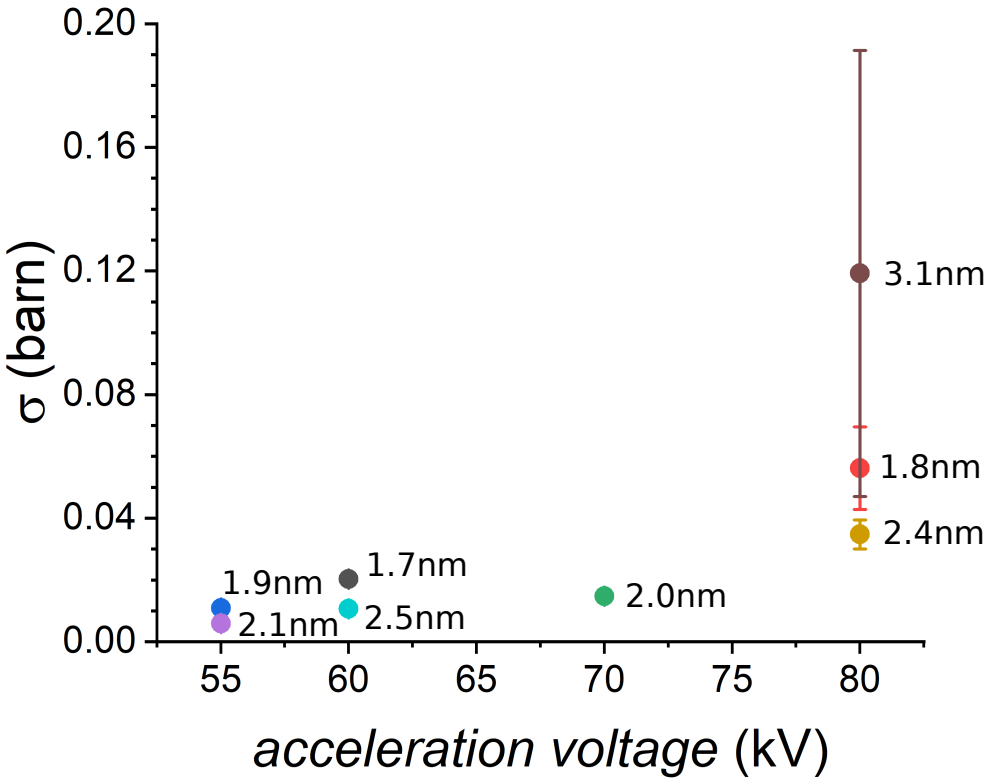

Figure 4.8: **Displacement cross sections at different FOVs.** Displacement cross sections for different accelerarion voltages and different FOVs.

The results for the displacement cross sections (barn) with the earlier mentioned acceleration

Table 4.3: Displacement Cross section with different Acc. voltage - FOV

Acc. voltage (kV)	FOV (nm)	σ (barn)	$\Delta\sigma$ (barn)
55	1.9	0.011	$\pm$0.00033
55	2.1	0.0059	$\pm$0.00017
60	1.7	0.020	$\pm$0.0010
60	2.5	0.011	$\pm$0.00036
70	2.0	0.015	$\pm$0.00083
80	1.8	0.056	$\pm$0.011
80	2.4	0.035	$\pm$0.0041
80	3.1	0.12	$\pm$0.045

voltages with different FOVs are plotted in Fig. 4.8, calculated according to equation 4.5 and the errors are listed in table 4.3.

In graphene which has a pure knock-on mechanism, the displacement cross section is independent of the FOV, however for hBN it looks like it might not be.

As the displacement cross section is a probability, it is more likely that damage occurs at lower FOV. Which means the more you zoomed in, the scanning area is smaller and can be damage faster which indicates that it is not a pure knock-on prcess. On the other hand a wide FOV damage slower, which could be explained that the electrons spread slightly more through the lattice. At

4.4.2 σ separately for B & N

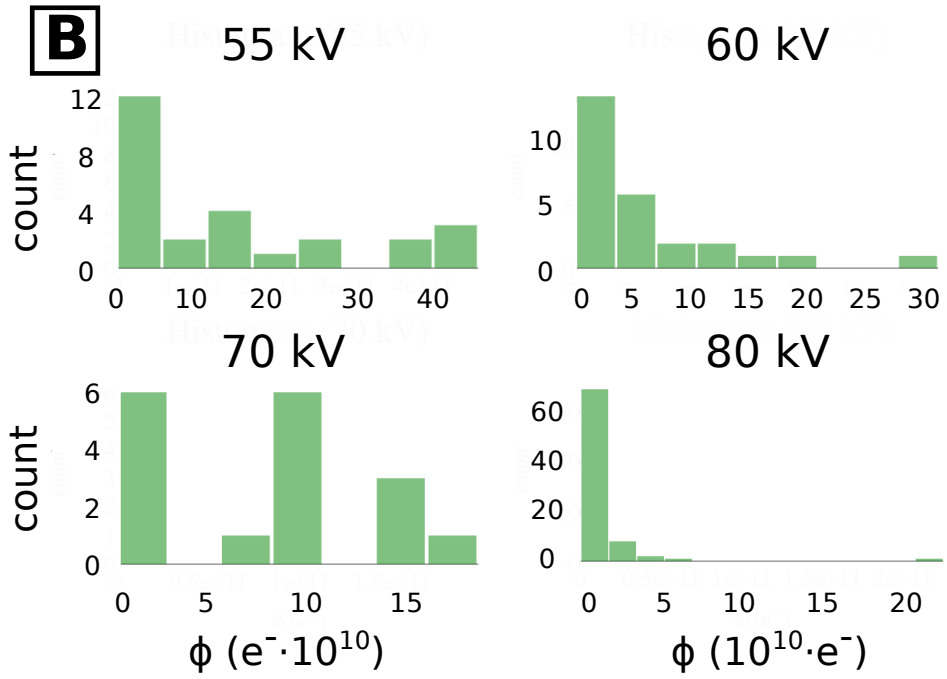

Figure 4.9: **Histograms of B electron doses.** B electron doses until first displacement for different acceleration voltages $55 - 80$ kV.

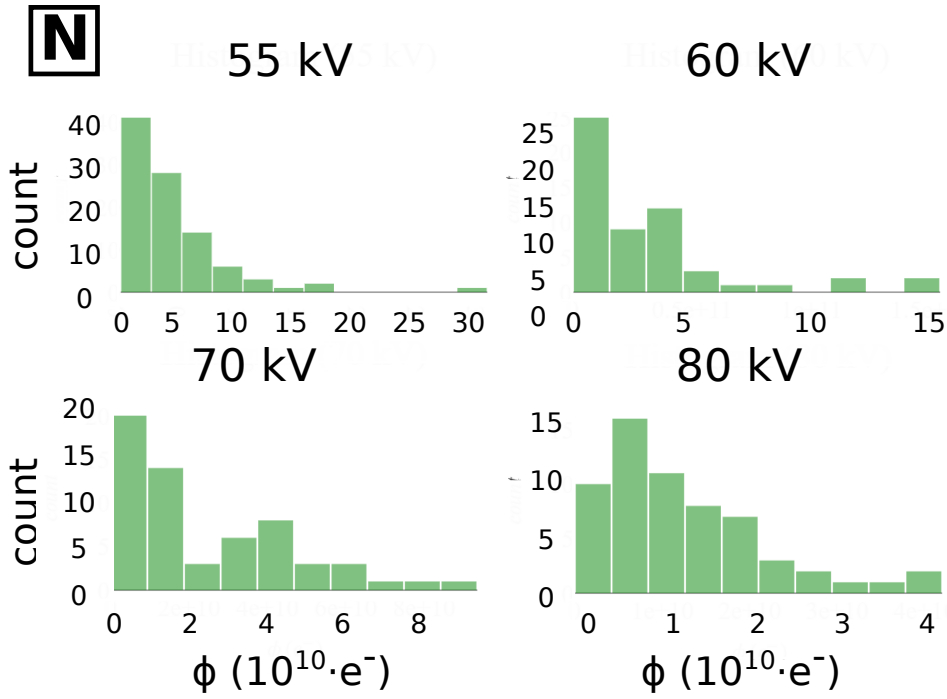

Figure 4.10: **Histograms of N electron doses.** N electron doses until first displacement for different acceleration voltages $55 - 80$ kV.

The histograms in Fig. 4.9 & 4.10 and the exponential distribution images in Fig. 4.11 & 4.12 were plotted with the same method as in the previous section. The difference here is that instead of different FOVs, calculations were done for boron and nitrogen separately. Some histograms don't show a Poisson distribution because of poor statistics. This is because we split the total number of experiments for one acceleration voltage into B and N. Also only single B and N vacancies were considered. The expectation value λ for boron and nitrogen separately at the acceleration voltages 55, 60, 70 and 80 kV are listed in table 4.4.

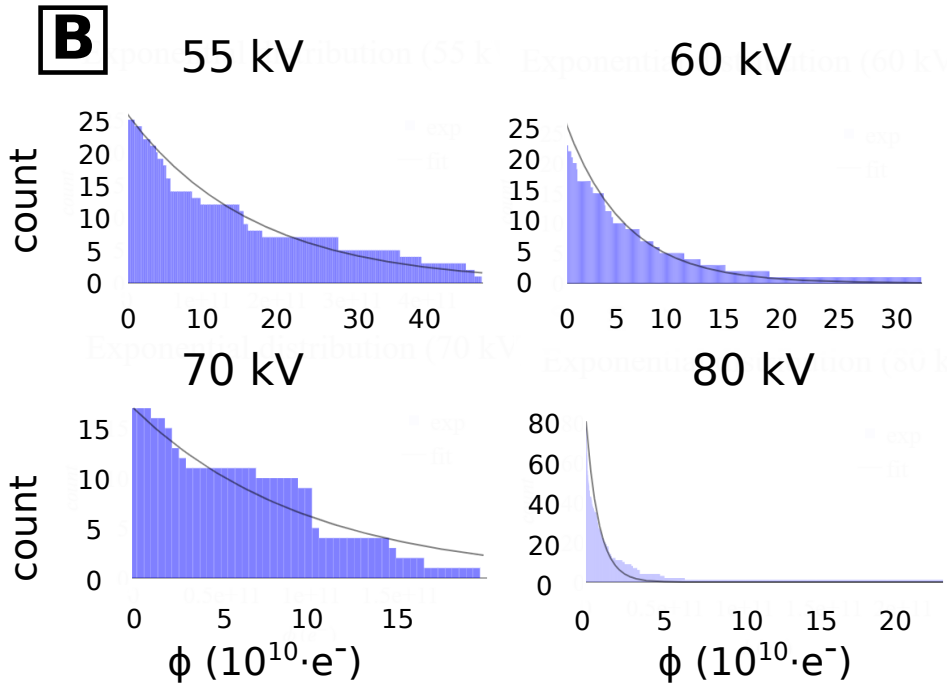

Figure 4.11: **Exponential distribution of B electron doses.** Exponential distribution with the expectation value λ as the fit (black solid line) for boron with different acceleration voltages.

Table 4.4: **Expectation values from for doses until first displacement separated for B and N.**

Acc. voltage (kV)	Element	λ ($\times 10^{10} e^-$) of dose until defect	$\Delta\lambda$ $\times 10^{10} e^-$
55	B	16.71	$\pm$0.35
55	N	4.21	$\pm$0.019
60	B	5.31	$\pm$0.12
60	N	2.92	$\pm$0.041
70	B	9.79	$\pm$0.42
70	N	2.55	$\pm$0.022
80	B	0.82	$\pm$0.018
80	N	1.29	$\pm$0.017

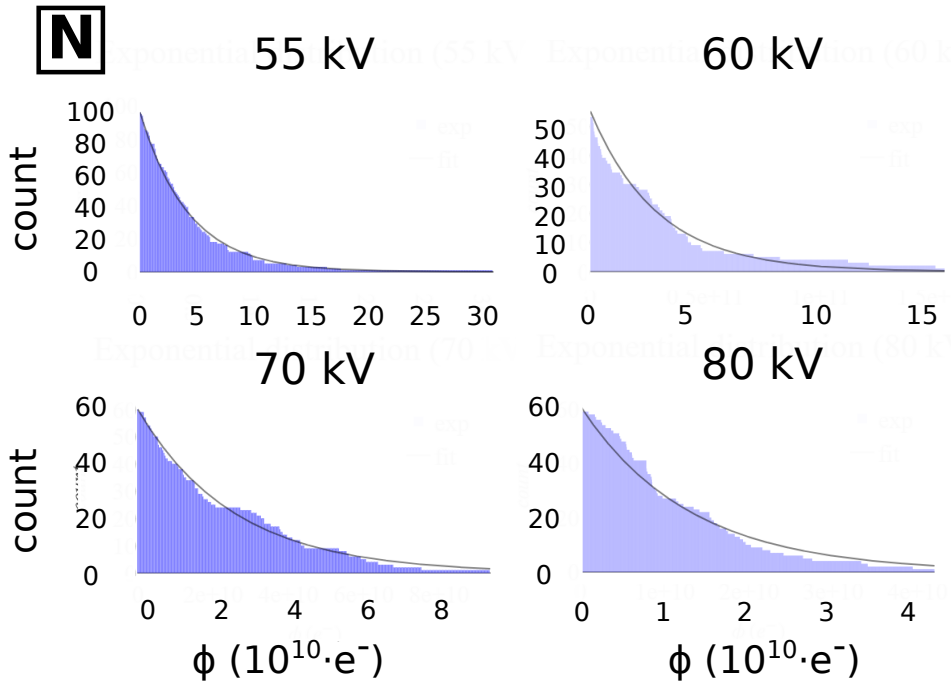

Figure 4.12: **Exponential distribution of N electron doses.** Exponential distribution with the expectation value λ as the fit (black solid line) for nitrogen with different acceleration voltages.

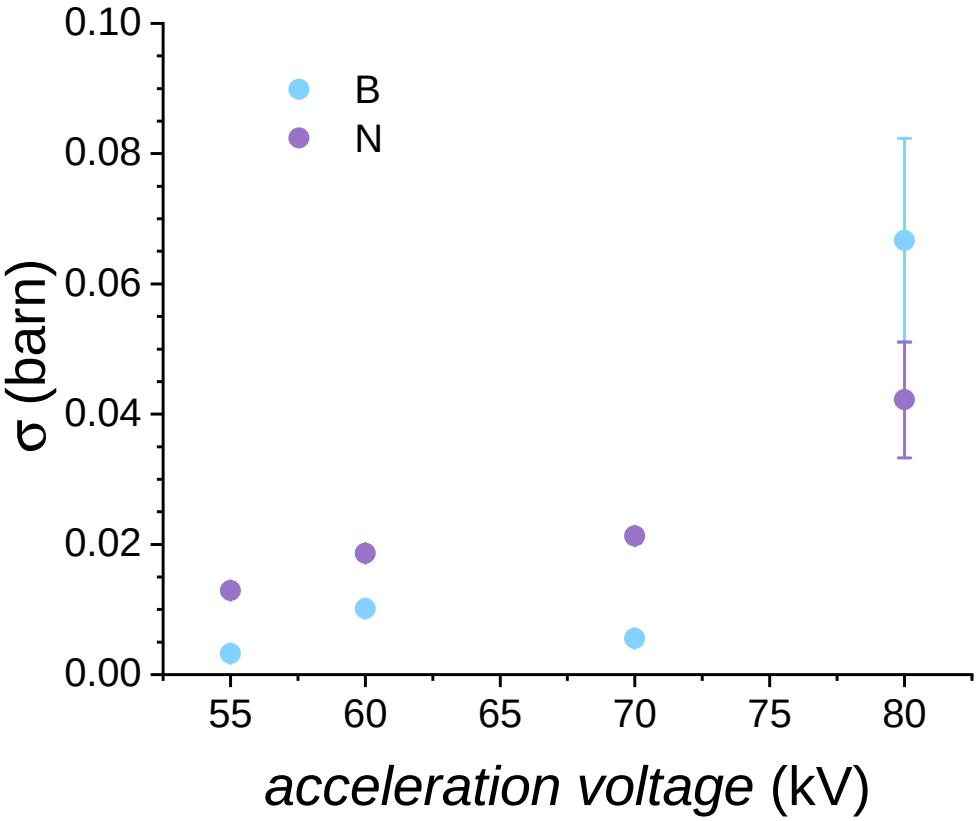

Figure 4.13: **Displacement cross sections separately for B and N.** Displacement cross sections (barn) for boron (blue) and nitrogen (violet) at different acceleration voltages (kV).

The results for the displacement cross section for boron (blue) and nitrogen (violet) as a function of acceleration voltage are plotted in Fig. 4.13. The displacement cross section values are listed with the errors for boron in table 4.5 and for nitrogen in table 4.6. For a pure knock-on event it is expected that the lighter atom is more likely to be kicked out from the lattice. In our case it is boron which is shown for the 80 kV measurements. But the plot shows the opposite at lower voltages. Here the nitrogen atom is statistically more favourable to be kicked out than boron. This indicates again an ionization damage process. As discussed earlier the knock-on mechanism dominates at higher energy.

To get a better understanding of the behaviour of B and N the percentage of single vacancies observed at each acceleration voltage is listed in table 4.7. Only the number of single vacancies of B and N were counted. At 55, 60 and 70 kV significantly more nitrogen atoms were kicked out than boron from the hBN lattice. However at 80 kV its the other way around, and more B

Table 4.5: **Displacement cross section of boron**

Acc. voltage (kV)	σ (barn)	$\Delta\sigma$ (barn)
55	0.0032	$\pm$0.000093
60	0.010	$\pm$0.00046
70	0.0055	$\pm$0.00024
80	0.066	$\pm$0.012

Table 4.6: **Displacement cross section of nitrogen**

Acc. voltage (kV)	σ (barn)	$\Delta\sigma$ (barn)
55	0.013	$\pm$0.00037
60	0.019	$\pm$0.00069
70	0.021	$\pm$0.0012
80	0.042	$\pm$0.0073

Table 4.7: **Percentage of N & B single vacancies**

Acc. voltage (kV)	B %	N %
55	21	79
60	33	67
70	22	78
80	57	43

atoms are ejected than the N atoms, but their percentages are not very far from each other. It appears that the nitrogen atoms seem to be more likely to be affected by the ionization damage mechanism than boron atoms.

4.5 Radiolysis

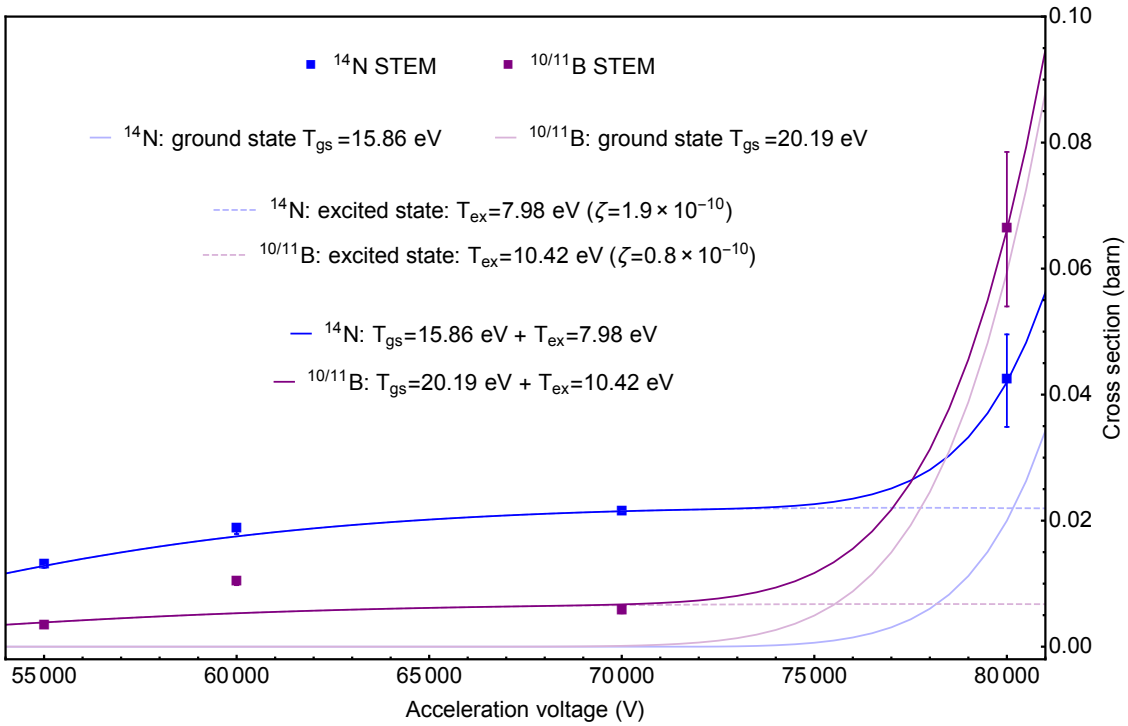

Figure 4.14: **Theoretical fit.** Theoretical fits for boron (blue) and nitrogen (violet) with the experimental datapoints. Work done with Alexandru Chirita (Fit courtesy: Alexandru Chirita).

A theoretical fit with a combination of the knock-on and ionization damage mechanism, as mentioned in section 3.2, [15], was done by Alexandru Chirita and is shown in Fig. 4.14 & 4.15. Experiment fit well with the theory. This supports the hypothesis that a combination of both mechanism play a role in hBN. Out of the fit we also get the threshold energy for the ground state $T_{gs}^{B} = 20.19$ eV for boron and $T_{gs}^{N} = 15.86$ eV for nitrogen. Compare this to the earlier calculated DFT simulated values by [11], with $T_{d}^{B} = 19.36$ eV for boron and $T_{d}^{N} = 23.06$ eV for nitrogen, there is a significant difference for nitrogen. On the other hand values for boron are very close to each other. Explanations for this could be that one excited state is sufficient for boron but not for nitrogen.

To explain the difference of the T_d's for N an additional process is needed to the in chapter 3.2.3

explained case with one excited state (equation 3.16). Expanding equation 3.16 with an addional second excited state $\sigma\left(E, T_d^{\text{exc2}}\right) \times \sigma_{\text{rad}}(E)$, we will get

$$\sigma_{\text{tot}}(E) = \sigma\left(E, T_d^{\text{gs}}\right) + \sigma\left(E, T_d^{\text{exc1}}\right) \times \sigma_{\text{rad}}(E) + \sigma\left(E, T_d^{\text{exc2}}\right) \times \sigma_{\text{rad}}(E). \tag{4.8}$$

Figure 4.15 shows theoretical fits with the experimental datapoints using equation 3.17. To get a better understaning of the connections between the ground state and the excited states, two fits were done with different numbers. One is the solid orange line with a ground state threshold energy of $T_{\text{gs}} = 15.86$ eV. The other one is the violet solid line with $T_{\text{gs}} = 23.06$ eV. Now the earlier mentioned DFT simulated threshold energy value for N ($T_d^N = 23.06$) fits. With the four experimental datapoints we cannot see a difference between those two fits. Additional experimental datapoints, espacially at voltages higher than 80 kV or even between 70 kV to 80 kV, will help us to get a better understanding of this new process.

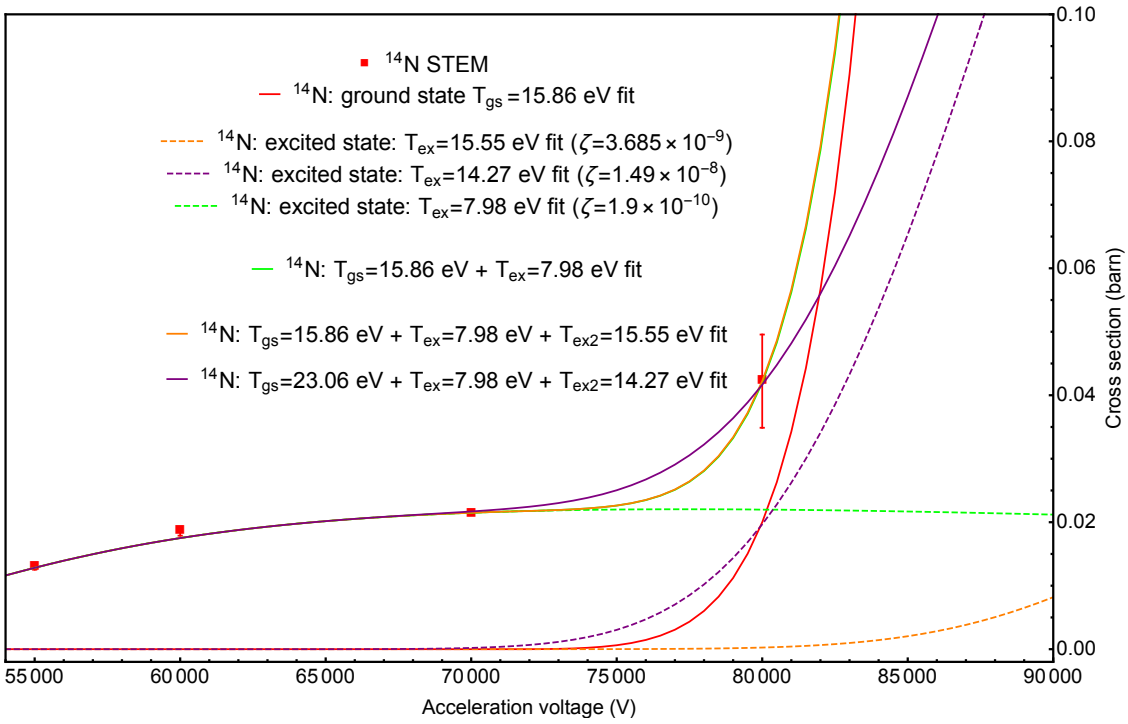

Figure 4.15: **Theoretical fit.** Theoretical fits for nitrogen with the experimental datapoints. Work done with Alexandru Chirita (Fit courtesy: Alexandru Chirita).

Chapter 5

Conclusions

The purpose of this work was to get a better understanding of the interaction of the insulating hBN and 2D materials in general with energetic electrons. Experimental work was needed to get a fundamental understanding of the properties and behaviour of hBN under an electron beam and its related damage mechanisms.

For scanning transmission electron microscopy experiments, sample preparation was required. Chemical vapor deposition grown hBN on top of a copper foil was transferred carefully onto a TEM grid. To obtain useable samples, a chemical etching process and a cleaning process afterwards was done.

Atomic resolution imaging made an analysis of single atom defects in hBN possible. Statistical analysis gives us information about electron dose rates and the probability of a displacement in terms of a discplacement cross section σ. To get this displacement cross section an exponential distribution of the dose until first defect from a Poisson process has been calculated. The already mentioned displacement cross section for this scattering process has been used to compare experimental data with theoretical predictions. In addition, interestingly, we also showed a new behaviour where N atoms get ejected occasionally as first vacancy in the frame, which was not expected to based on the theory.

We analysed two main properties to demonstrate that an additional ionization damage to the knock-on damage is also responsible for creating defects in hBN. One was at each acceleration voltage, different field of views (FOVs) and the other one was the two elements boron and nitrogen separately. We were able to show that at lower acceleration voltages radiolysis was dominant but both mechanisms play a role. However more experimental datapoints at different acceleration

voltages will improve the theoretical fit and will give a better understanding of the ionization damage process.

So far the analysis of the images was done manually. A better and more accurate way to analyse them would be a computer-assisted method. A new developed python machine-learning program can be trained for this purpose. Even if the resolution of the image is not good enough to manually identify the defect position, the program can still analyse it. It will not only allow to scan faster in real time but also can control the dose on individual atoms, which could reveal the unexpected dynamics in hBN or any 2D materials. Further, it could be more helpful in handling the large amount of data and their efficient analysis.

Bibliography

[1] Novoselov, K. S. *et al.* Electric Field Effect in Atomically Thin Carbon Films. *Science* **306**, 666–669 (2004). DOI: 10.1126/science.1102896.

[2] Mermin, N. D. & Wagner, H. Absence of Ferromagnetism or Antiferromagnetism in One- or Two-Dimensional Isotropic Heisenberg Models. *Physical Review Letters* **17**, 1133–1136 (1966). DOI: 10.1103/physrevlett.17.1133.

[3] Novoselov, K. S. *et al.* Two-dimensional atomic crystals. *Proceedings of the National Academy of Sciences* **102**, 10451–10453 (2005). DOI: 10.1073/pnas.0502848102.

[4] Coleman, J. N. *et al.* Two-Dimensional Nanosheets Produced by Liquid Exfoliation of Layered Materials. *Science* **331**, 568–571 (2011). DOI: 10.1126/science.1194975.

[5] Radisavljevic, B., Radenovic, A., Brivio, J., Giacometti, V. & Kis, A. Single-layer MoS2 transistors. *Nature Nanotechnology* **6**, 147–150 (2011). DOI: 10.1038/nnano.2010.279.

[6] Eda, G. *et al.* Photoluminescence from Chemically Exfoliated MoS2. *Nano Letters* **11**, 5111–5116 (2011). DOI: 10.1021/nl201874w.

[7] Kim, K. K. *et al.* Synthesis of Monolayer Hexagonal Boron Nitride on Cu Foil Using Chemical Vapor Deposition. *Nano Letters* **12**, 161–166 (2011). DOI: 10.1021/nl203249a.

[8] Zhan, Y., Liu, Z., Najmaei, S., Ajayan, P. M. & Lou, J. Large-Area Vapor-Phase Growth and Characterization of MoS2Atomic Layers on a SiO2Substrate. *Small* **8**, 966–971 (2012). DOI: 10.1002/smll.201102654.

[9] Komsa, H.-P. *et al.* Two-Dimensional Transition Metal Dichalcogenides under Electron Irradiation: Defect Production and Doping. *Phys. Rev. Lett.* **109**, 035503 (2012). DOI: 10.1103/PhysRevLett.109.035503.

[10] Zhang, J. *et al.* Point defects in two-dimensional hexagonal boron nitride: A perspective. *Journal of Applied Physics* **128**, 100902 (2020). DOI: 10.1063/5.0021093.

[11] Kotakoski, J., Jin, C. H., Lehtinen, O., Suenaga, K. & Krasheninnikov, A. V. Electron knock-on damage in hexagonal boron nitride monolayers. *Phys. Rev. B* **82**, 113404 (2010). DOI: 10.1103/PhysRevB.82.113404.

[12] Kumar, R., Parashar, A. & Mertiny, P. Displacement thresholds and knock-on cross sections for hydrogenated h-BN monolayers. *Computational Materials Science* **142**, 82–88 (2018). DOI: 10.1016/j.commatsci.2017.10.001.

[13] Zobelli, A., Gloter, A., Ewels, C. P., Seifert, G. & Colliex, C. Electron knock-on cross section of carbon and boron nitride nanotubes. *Physical Review B* **75** (2007). DOI: 10.1103/physrevb.75.245402.

[14] Susi, T., Meyer, J. C. & Kotakoski, J. Quantifying transmission electron microscopy irradiation effects using two-dimensional materials. *Nature Reviews Physics* **1**, 397–405 (2019). DOI: 10.1038/s42254-019-0058-y.

[15] Kretschmer, S., Lehnert, T., Kaiser, U. & Krasheninnikov, A. V. Formation of Defects in Two-Dimensional MoS_2 in the Transmission Electron Microscope at Electron Energies below the Knock-on Threshold: The Role of Electronic Excitations. *Nano Letters* **20**, 2865–2870 (2020). DOI: 10.1021/acs.nanolett.0c00670.

[16] Egerton, R. F. Mechanisms of radiation damage in beam-sensitive specimens, for TEM accelerating voltages between 10 and 300 kV. *Microscopy Research and Technique* **75**, 1550–1556 (2012). DOI: 10.1002/jemt.22099.

[17] Meyer, J. C. *et al.* Accurate Measurement of Electron Beam Induced Displacement Cross Sections for Single-Layer Graphene. *Phys. Rev. Lett.* **108**, 196102 (2012). DOI: 10.1103/PhysRevLett.108.196102.

[18] Krivanek, O. L. *et al.* An electron microscope for the aberration-corrected era. *Ultramicroscopy* **108**, 179–195 (2008). DOI: 10.1016/j.ultramic.2007.07.010.

[19] Susi, T. *et al.* Isotope analysis in the transmission electron microscope. *Nature Communications* **7** (2016). DOI: 10.1038/ncomms13040.

[20] Mermin, N. D. Crystalline Order in Two Dimensions. *Physical Review* **176**, 250–254 (1968). DOI: 10.1103/PhysRev.176.250.

[21] Liu, L., Feng, Y. P. & Shen, Z. X. Structural and electronic properties of *h* -BN. *Physical Review B* **68**, 104102 (2003). DOI: 10.1103/PhysRevB.68.104102.

[22] Alem, N. *et al.* Atomically thin hexagonal boron nitride probed by ultrahigh-resolution transmission electron microscopy. *Physical Review B* **80**, 155425 (2009). DOI: 10.1103/PhysRevB.80.155425.

[23] Chen, C. *et al.* Misfit accommodation mechanism at the heterointerface between diamond and cubic boron nitride. *Nature Communications* **6**, 6327 (2015). DOI: 10.1038/ncomms7327.

[24] Doni, E. & Parravicini, G. P. Energy bands and optical properties of hexagonal boron nitride and graphite. *Il Nuovo Cimento B (1965-1970)* **64**, 117–144 (1969). DOI: 10.1007/BF02710286.

[25] Watanabe, K., Taniguchi, T. & Kanda, H. Direct-bandgap properties and evidence for ultraviolet lasing of hexagonal boron nitride single crystal. *Nature Materials* **3**, 404–409 (2004). DOI: 10.1038/nmat1134.

[26] Falin, A. *et al.* Mechanical properties of atomically thin boron nitride and the role of interlayer interactions. *Nature Communications* **8**, 15815 (2017). DOI: 10.1038/ncomms15815.

[27] Graphene Supermarket :: 2. Research Materials :: 1. Boron Nitride (BN) :: CVD hBN on copper foil :: Single layer h-BN (Boron Nitride) film grown on copper foil: 2" x 1". https://graphene-supermarket.com/Single-layer-h-BN-Boron-Nitride-film-grown-in-copper-foil-2-x-1.html.

[28] Williams, . C. *Transmission Electron Microscopy: A Textbook for Materials Science* (Springer, 2009), second edn.

[29] Erni, R. *Aberration-Corrected Imaging in Transmission Electron Microscopy: An Introduction* (IMPERIAL COLLEGE PRESS, 2010).

[30] Brydson, R. (ed.) *Aberration-Corrected Analytical Transmission Electron Microscopy* (John Wiley & Sons, Ltd, 2011).

[31] Smith, D. J. Ultimate resolution in the electron microscope? *Materials Today* **11**, 30–38 (2008). DOI: 10.1016/S1369-7021(09)70005-7.

[32] Crewe, A. V. Scanning Electron Microscopes: Is High Resolution Possible? *Science* **154**, 729–738 (1966). DOI: 10.1126/science.154.3750.729.

[33] Tripathi, M. *Modifying Low-Dimensional Materials Using Energetic Charged Particles*. Ph.D. thesis, Wien (2019).

[34] Hillyard, S. & Silcox, J. Detector geometry, thermal diffuse scattering and strain effects in ADF STEM imaging. *Ultramicroscopy* **58**, 6–17 (1995). DOI: 10.1016/0304-3991(94)00173-K.

[35] Pennycook, S. & Jesson, D. High-resolution Z-contrast imaging of crystals. *Ultramicroscopy* **37**, 14–38 (1991). DOI: 10.1016/0304-3991(91)90004-P.

[36] Krivanek, O. L. *et al.* Atom-by-atom structural and chemical analysis by annular dark-field electron microscopy. *Nature* **464**, 571–574 (2010). DOI: 10.1038/nature08879.

[37] Egerton, R. F., Li, P. & Malac, M. Radiation damage in the TEM and SEM. *Micron* **35**, 399–409 (2004). DOI: 10.1016/j.micron.2004.02.003.

[38] Leuthner, G. T. *et al.* Scanning transmission electron microscopy under controlled low-pressure atmospheres. *Ultramicroscopy* **203**, 76–81 (2019). DOI: 10.1016/j.ultramic.2019.02.002.

[39] McKinley, W. A. & Feshbach, H. The Coulomb Scattering of Relativistic Electrons by Nuclei. *Physical Review* **74**, 1759–1763 (1948). DOI: 10.1103/PhysRev.74.1759.

[40] Mott, N. The polarisation of electrons by double scattering. *Proceedings of the Royal Society of London. Series A, Containing Papers of a Mathematical and Physical Character* **135**, 429–458 (1932). DOI: 10.1098/rspa.1932.0044.

[41] Bethe, H. Zur Theorie des Durchgangs schneller Korpuskularstrahlen durch Materie. *Annalen der Physik* **397**, 325–400 (1930). DOI: 10.1002/andp.19303970303.

[42] Jiang, N. & Spence, J. C. On the dose-rate threshold of beam damage in TEM. *Ultramicroscopy* **113**, 77–82 (2012). DOI: 10.1016/j.ultramic.2011.11.016.

[43] Bamberg, G., Baur, F. & Krapp, M. *Statistik: Eine Einführung Für Wirtschafts- Und Sozialwissenschaftler* (De Gruyter Oldenbourg, 2017).

[44] Gross, R. & Marx, A. *Festkörperphysik* (De Gruyter Oldenbourg, 2014).